OBSERVATION AND MEASUREMENT OF THE HIGGS-LIKE BOSON AT 125 GEV IN THE TWO-PHOTON DECAY CHANNEL WITH THE CMS EXPERIMENT

XIAOHANG QUAN

A DISSERTATION

PRESENTED TO THE FACULTY

OF PRINCETON UNIVERSITY

IN CANDIDACY FOR THE DEGREE

OF DOCTOR OF PHILOSOPHY

RECOMMENDED FOR ACCEPTANCE

BY THE DEPARTMENT OF

PHYSICS

ADVISOR: CHRISTOPHER G. TULLY

SEPTEMBER, 2013

Abstract

We present results for the search for the Standard Model Higgs boson in the two-photon channel using the full 2011+2012 dataset recorded by the CMS experiment at the LHC. The MVA analysis, most sensitive for discovery, observes an excess of events at 125 GeV with a local significance of 3.2σ. The mass of the observed boson is measured to be $125.4 \pm 0.5(stat.) \pm 0.6(syst.)$ GeV. For a Higgs boson mass hypothesis of 125 GeV, the best fit signal strength is $0.78^{+0.28}_{-0.26}$ times the SM Higgs boson cross-section. An upper limit on its natural width is found to be 6.9 GeV/c^2 at 95% confidence level.

We also present results from searches for an additional Higgs boson decaying into two photons, treating the observed resonance as a background process. Cases in which the additional state is SM-like, fermiophobic or gauge-phobic have been considered. In addition, we present a search targeted at discriminating between a single Higgs boson at 125 GeV and two very close-by ones.

Acknowledgements

I would like to express my deepest and most sincere gratitude to my advisor, Professor Christopher Tully. His generous help and unfailing patience throughout my career at Princeton made this dissertation possible. He has been the best advisor that I could have hoped for, and his guidance has enlightened me not only within the field of physics but also in life. The experiences I have gained working with him have had life-changing influence on me.

I am deeply indebted to the faculty of the Princeton Physics Department. The courses I took with them and the various discussions and interactions that I have had with them kindled my passion for physics and helped me grow as a physicist as well as an individual. I wish to especially thank Professors Robert Austin, Christiano Galbiati, Steve Gubser, David Huse, Igor Klebanov, Daniel Marlow, Chiara Nappi, Jim Olsen, Pierre Piroue, Alexander Polyakov, Michael Romalis, Joseph Taylor, Herman Verlinde, Ali Yazdani and many more. During the past eight years, the Department has also given me innumerable unthinkably wonderful opportunities to learn, research and experience. This dissertation and myself owe much to the Department. Outside the Physics Department, I would also like to thank all of the professors that have taught me during my eight years at Princeton, especially Professor Erhan Çinlar for his continuous support and advice.

I would also like to express my earnest gratitude to my colleagues from the Higgs group (especially $H \to \gamma\gamma$), the ECAL group and the Trigger group at CMS. It has truly been an honor to collaborate with them. I treasure our shared journey from 2009 through the Higgs discovery on July 4th, 2012, past HCP2012, and finally until LP2013. I wish to thank Doug Berry, Jim Branson, Bob Cousins, Andre David, Jonathan Hollar, Andre Holzner,

Matt Kenzie, Paolo Meridiani, Pasquale Musella, Shervin Nourbakhsh, Chris Palmer, Pedro Parracho, Christoph Paus, Giovanni Petrucciani, Marco Pieri, Vladimir Rekovic, Matteo Sani, Chris Seez, Alessandro Thea, Scott Thomas, Nick Wardle and many more.

This dissertation would not have been possible without the contributions from all CMS collaboration members, to whom I express my deep gratitude.

I would like to thank all my friends at CERN for their company and support. I wish to especially thank Halil Saka and Andrzej Zuranski for their friendship throughout the years I spent at CERN.

Lastly, I wish to thank my parents, Mr. Hongjun Quan and Mrs. Xinhang Yan, for their twenty-six years of unconditional caring and love. This dissertation would not have been possible without the opportunities, educational and otherwise, they provided me. To them I dedicate this dissertation.

Contents

List of Figures

List of Tables

Chapter 1

The Standard Model and the Higgs Boson

The Standard Model (SM) describes all known elementary particles and the electromagnetic, weak and strong interactions between them [3, 4, 5]. All particles are interpreted as excitations of relativistic quantum fields. Matter is described in terms of spin-1/2 fermions. Elementary particles interact with each other via exchanges of gauge bosons, also called the mediators of the corresponding fields.

1.1 Elementary Particles and Forces

There are three generations of spin-1/2 fermions. Each generation is comprised of two quarks and two leptons (up-type and down-type). For each fermion, there exists an anti-particle with exactly the same properties modulo an opposite electric charge. A schematic view of the Standard Model constituents is shown in Figure 1.1.

All particles with electric charge experience the electromagnetic force. Its mediator is the massless photon, which has infinite range. The theory which describes the electromagnetic interaction is called Quantum Electrodynamics (QED).

The strong force is mediated by massless gluons. Both quarks and gluons experience

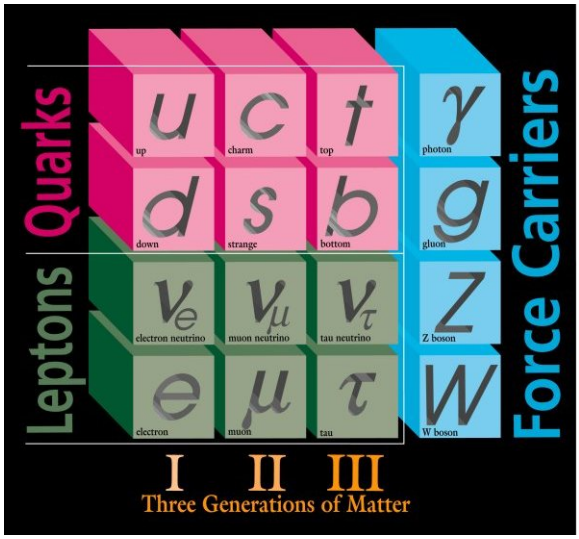

Figure 1.1: A schematic view of the Standard Mode constituents.

the strong force. The theory which describes the strong force is called Quantum Chromodynamics (QCD). The strong coupling constant α_s becomes weaker at higher energies (i.e. smaller distances). This property is responsible for the effect called the quark confinement, which explains why individual quarks cannot be observed in nature. Quarks can either bind in three to constitute baryons, or in quark and anti-quark pairs to constitute mesons. In large part, the binding energy of quarks confined inside protons and neutrons accounts for the mass of these composite particles. The equivalent of the electric charge in the context of QCD is the color charge, which is carried by both quarks and gluons.

The weak force affects all fermions and is mediated by the W and Z bosons. Unlike the electromagnetic and strong forces, the weak force is chiral-dependent and differentiates between left-handed and right-handed fermions. It can also change the flavor of quarks. Because of its heavy mediator bosons, the weak force has a very short range (less than 10^{-16} m). The weak and electromagnetic forces, despite their seeming differences, originate from the same symmetry - the electroweak symmetry.

The generation of the W and Z masses, along with the differentiation of the electroweak force in the electromagnetic and weak interactions, is the main motivation for introducing a Higgs boson in the Standard Model.

1.2 Gauge Symmetries

The Standard Model is a gauge group of $SU(3)_c \times SU(2)_L \times U(1)_Y$, which accounts for the strong, electromagnetic and weak interactions. The latter two forces are unified in the electroweak theory. The gauge invariance of $SU(2)_L \times U(1)_Y$ demands that the gauge bosons have zero mass, since a term like $m^2 A_\mu A^\mu$ is not invariant under the transformation $A_\mu \rightarrow A_\mu - \partial_\mu \chi$ where χ is a function of position in 4-vector space. This contradicts with experimentally observed non-zero W and Z masses. This contradiction is solved by introducing the Higgs mechanism into the Standard Model.

1.3 The Higgs Mechanism

1.3.1 A Simple Abelian Case

To illustrate the core physics of the Higgs mechanism, we first review a simple Abelian case of a complex scalar boson ϕ and a massless gauge boson A_μ. The Lagrangian can be generally written as [13]:

$$\mathcal{L} = (D_\mu \phi^*)(D^\mu \phi) + \mu^2 \phi^* \phi - \lambda(\phi^* \phi)^2 - \frac{1}{4} F^{\mu\nu} F_{\mu\nu}, \tag{1.1}$$

$$F^{\mu\nu} = \partial^\mu A^\nu - \partial^\nu A^\mu, \tag{1.2}$$

$$D^\mu = \partial^\mu + iqA^\mu. \tag{1.3}$$

The theory is invariant under local gauge transformation:

$$\phi \rightarrow e^{iq\alpha(x)} \phi, \tag{1.4}$$

$$A^\mu \rightarrow A^\mu - \partial_\mu \alpha(x). \tag{1.5}$$

When the local symmetry is broken, $\alpha(x)$ can be set to 0 without loss of generality, and consequently it is eliminated from the physical spectrum by the above gauge invariance, resulting only in a massless Goldstone boson. Now ϕ becomes a real field with minimum

value at $\phi_0 = \nu/\sqrt{2} = \sqrt{\mu^2/2\lambda}$. We can expand it around its minimum as $\phi = [\nu+\varphi(x)]/\sqrt{2}$, where $\varphi(x)$ is a real field. The Lagrangian now becomes

$$\begin{aligned}\mathcal{L} = &\frac{1}{2}[(\partial_\mu - iqA_\mu)(\nu+\varphi)(\partial^\mu + iqA^\mu)(\nu+\varphi)] \\ &+\frac{1}{2}\mu^2(\nu+\varphi)^2 - \frac{1}{4}\lambda(\nu+\varphi)^4 - \frac{1}{4}F^{\mu\nu}F_{\mu\nu}.\end{aligned} \tag{1.6}$$

We recognize a mass term for the gauge boson: $(q^2\nu^2/2)A_\mu A^\mu$. The mass term for the scalar boson is $-\lambda\nu^2\varphi^2$. Various other terms describe the interaction between A and φ and the self-interaction of φ. This translation from a theory with a complex scalar boson and a massless gauge boson into one with a real scalar boson and a massive gauge boson is called the Higgs mechanism.

1.3.2 The Higgs Mechanism in the Standard Model

The situation in the Standard Model is similar, with the gauge group $SU(2) \times U(1)$. After the breaking of the electroweak symmetry, there exists a real scalar field and the corresponding quantum is the experimentally observable Higgs boson [6, 7, 8, 9, 10, 11].

There are three gauge bosons A^a_μ associated with $SU(2)$ and one gauge bosons B_μ associated with $U(1)$. Assume their gauge couplings are g and g' respectively. In the Lagrangian, the covariant derivative is now[12]:

$$D_\mu = \partial_\mu - igT^aA^a_\mu - ig'SB_\mu \tag{1.7}$$

where T^a are the $SU(2)$ generators and S is the charge of the particle relative to the $U(1)$ group. The Higgs boson ϕ is an $SU(2)$ doublet. Its S is defined to be $1/2$ and its T^a is $\sigma^a/2$. As before, we have the freedom to choose the gauge such that

$$\phi \to \frac{1}{\sqrt{2}}(\nu + \varphi(x)). \tag{1.8}$$

We can call

$$W^\pm_\mu = A^\pm_\mu, Z^0_\mu = A^3_\mu \cos\theta_W - B_\mu \sin\theta_W. \tag{1.9}$$

Then we have:

$$m_W = g\nu/2, \tag{1.10}$$

$$m_Z = \frac{\sqrt{(g^2 + g'^2)}}{g} m_W = \cos\theta_W m_W. \tag{1.11}$$

The other orthogonal combination of A^3_μ and B_μ,

$$A_\mu = A^3_\mu \sin\theta_W + B_\mu \cos\theta_W \tag{1.12}$$

remains massless, and is identified as the photon.

1.4 Standard Model Higgs Production Mechanisms and Decays

In the Standard Model, Higgs boson production in proton-proton collisions include four main mechanisms: gluon fusion ($gg \to H$), vector boson fusion ($qq \to H$ + 2 jets), associated production of a Higgs boson with a W or Z boson, and associated production with a $t\bar{t}$ pair [14, 15]. Figure 1.2 shows the Feynman diagrams for these four production mechanisms.

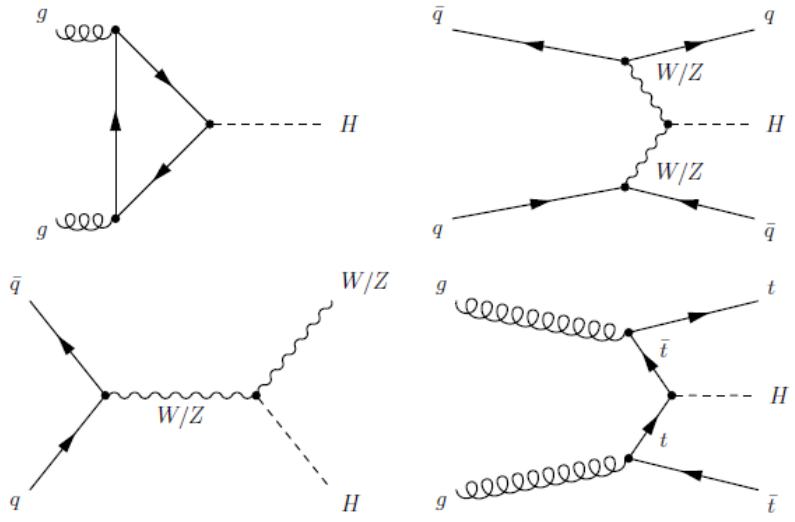

Figure 1.2: Feynman diagrams for the four main production mechanisms of the Standard Model Higgs boson at the LHC.

Figure 1.3 shows the cross section of each mechanism as a function of the Higgs boson mass at $\sqrt{s} = 7$ TeV and 8 TeV.

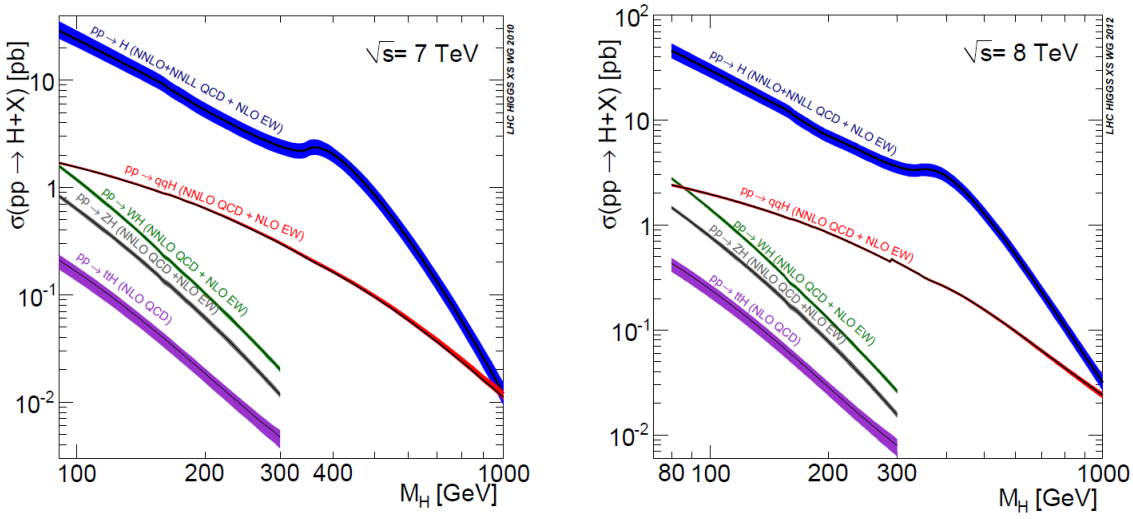

Figure 1.3: Theoretical predictions for the Higgs boson production cross sections in proton-proton collisions at $\sqrt{s} = 7$ TeV (left) and 8 TeV (right) [16, 17].

At leading order, the Standard Model Higgs boson can decay into pairs of fermions and W or Z bosons. Since the coupling of the Standard Model Higgs boson to fermions is proportional to the fermion mass, the decay branching ratio to any fermion is proportional to the square of its mass. Therefore, for m_H below the $2m_t$ threshold, the primary fermionic decay products are $b\bar{b}$ pairs, with smaller contributions from $c\bar{c}$ and $\tau\tau$ pairs. For the bosonic decays, for m_H below the $2m_W$ or $2m_Z$ threshold, the Higgs boson can decay into a pair of off-shell W's or Z's, which subsequently decay into four leptons. Loop-induced decay into a pair of photons or gluons are also important in the low-mass region. The Higgs boson can decay into two photons via a fermion loop, dominated by the top quark contribution, and via a W loop (Figure 1.4) [18]. The various Higgs boson decay branching fractions as functions of m_H are shown in Figure 1.5.

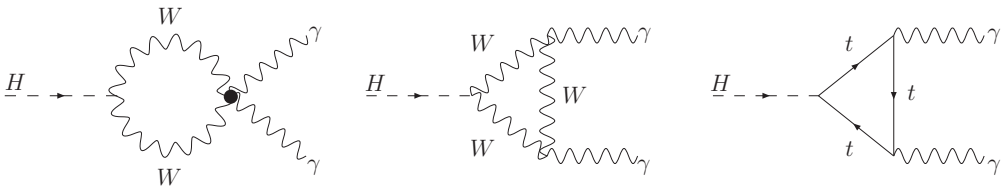

Figure 1.4: Leading order Feynman diagrams for a Standard Model Higgs boson decaying into two photons.

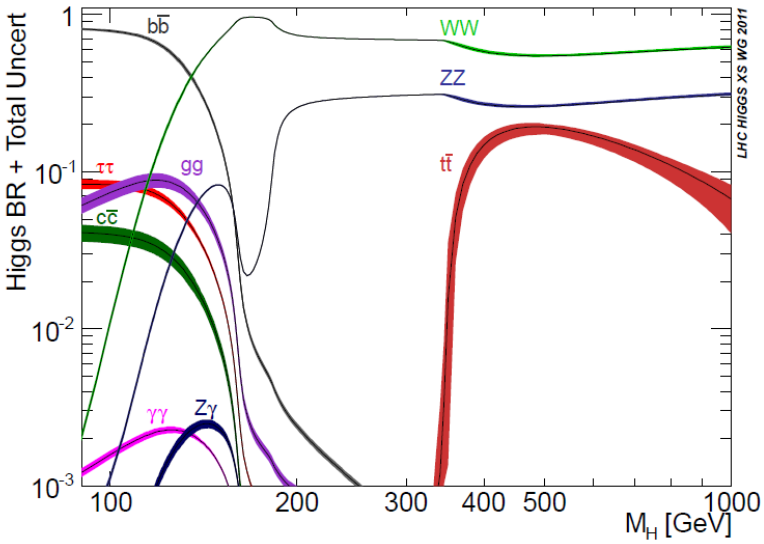

Figure 1.5: Theoretical predictions for the Higgs boson decay branching fractions. Theoretical uncertainties are displayed using bands [16, 17].

1.5 Bounds on the Higgs Boson Mass

Although the Higgs boson mass is a free parameter in the Standard Model framework, some constraints can be determine from theoretical assumptions and experimental measurements.

An upper bound on the Higgs boson mass results from the unitarity constraints on the Higgs sector [13]. Consider the scattering amplitude for $W_L^+W_L^- \to W_L^+W_L^-$ in the limit where the Higgs mass is much greater than m_W, then we have:

$$A(W_L^+W_L^- \to W_L^+W_L^-) = -\sqrt{2}G_F m_H^2[\frac{s}{s-m_H^2} + \frac{t}{t-m_H^2}]. \tag{1.13}$$

Then, the contribution to the $J = 0$ partial wave is:

$$\begin{aligned} a_0 &= \frac{1}{16\pi s}\int_{-s}^{0} A dt \\ &= -\frac{G_F m_H^2}{8\pi\sqrt{2}}[2 + \frac{m_H^2}{s - m_H^2} - \frac{m_H^2}{s}\ln(1 + \frac{s}{m_H^2})]. \end{aligned}$$

For $s \gg m_H^2$, $a_0 = -\frac{G_F m_H^2}{4\pi\sqrt{2}}$. Partial wave unitarity requires

$$| a_0 |^2 \leq | \Im(a_0) |, \tag{1.14}$$

which implies that

$$| \Re(a_0) | \leq \frac{1}{2}, m_H^2 \leq \frac{4\pi\sqrt{2}}{3G_F} \simeq (700 \text{ GeV})^2. \tag{1.15}$$

Further bounds on the Higgs boson mass can be obtained by requiring that the running quartic Higgs coupling [13]:

$$\lambda(Q) = \frac{\lambda(\nu)}{1 - \frac{3\lambda(\nu)}{4\pi^2}\ln(\frac{Q^2}{\nu^2})} \tag{1.16}$$

remains finite up to the Plank scale $\Lambda \simeq 10^{19}$ GeV, from which we obtain the limit $m_H \lesssim$ 140 GeV. This is called the "triviality bound".

A lower bound on the Higgs boson mass is found by requiring that λ remains positive after the inclusion of radiative corrections, i.e. the minimum of the Higgs potential is an absolute minimum. This is called the "vacuum stability bound". A looser bound of similar construction is obtained by requiring that the minimum is local instead of absolute. This is called the "metastability bound". Figure 1.6 shows these lower limits with their uncertainties in bands.

Apart from theoretical calculations, constraints on the Higgs boson mass arise also from measurements of other electroweak observables at various past experiments and global fits of the SM. Figure 1.7 shows the $\Delta\chi^2$ of the fit to the electroweak precision measurements performed at LEP, SLC and Tevatron as of 2011. The yellow regions have been excluded by direct searches at LEP and Tevatron.

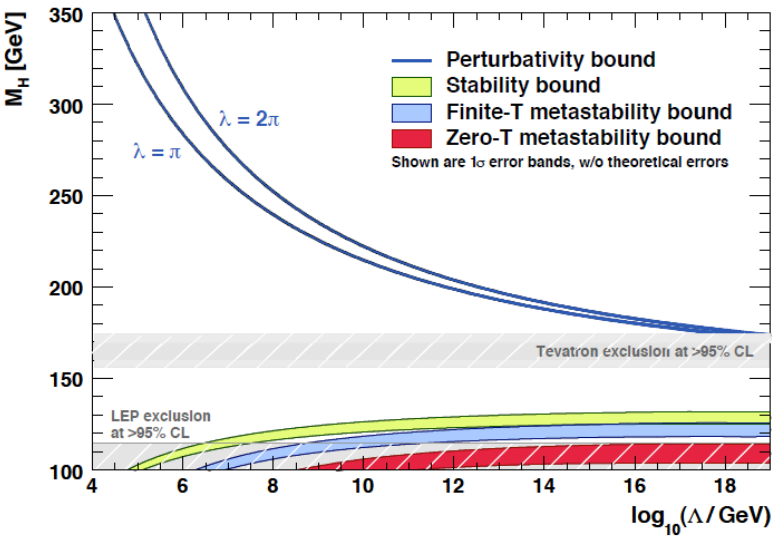

Figure 1.6: Lower bounds on the Higgs boson mass as functions of the cut-off scale Λ [19].

1.6 Extension of the Standard Model

Up until now we have only discussed the simplest electroweak symmetry breaking mechanism, where the Higgs sector is comprised of only one physical neutral Higgs scalar. Given the fact that there is no physical requirement for the minimal choice, it is natural to look beyond into the extended Higgs sector. One of the simplest possible extensions of the SM are the two-Higgs-doublet models (2HDMs), which are very well-motivated in a few ways. Some of the strongest motivations include supersymmetry, Baryongenesis and axion models [21, 22].

In a 2HDM extension, the general Higgs potential can be written as [13]:

$$V(\phi_1,\phi_2) = \lambda_1(\phi_1^\dagger\phi_1 - v_1^2)^2 + \lambda_2(\phi_2^\dagger\phi_2 - v_2^2)^2 \tag{1.17}$$

$$+\lambda_3[(\phi_1^\dagger\phi_1 - v_1^2) + (\phi_2^\dagger\phi_2 - v_2^2)]^2 \tag{1.18}$$

$$+\lambda_4[(\phi_1^\dagger\phi_1)(\phi_2^\dagger\phi_2) - (\phi_1^\dagger\phi_2)(\phi_2^\dagger\phi_1)] \tag{1.19}$$

$$+\lambda_5[\Re(\phi_1^\dagger\phi_2) - v_1v_2\cos\xi]^2 + \lambda_6[\Im(\phi_1^\dagger\phi_2) - v_1v_2\sin\xi]^2, \tag{1.20}$$

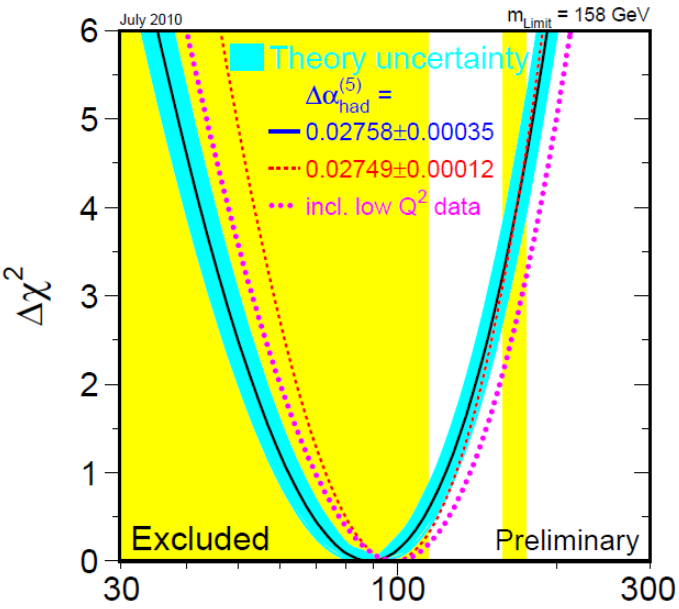

Figure 1.7: $\Delta\chi^2$ of the fit to the electroweak precision measurements performed at LEP, SLC and Tevatron as of 2011. The yellow regions have been excluded by searches at LEP and Tevatron [20].

where the λ's are real parameters. The mixing angle β is defined as:

$$\tan\beta = v_2/v_1. \tag{1.21}$$

There are five physical Higgs bosons in this model: a charged doublet ($H^{\pm}$); two neutral CP-even scalars (H^0 and h^0); a neutral CP-odd scalar (A^0), often called a pseudoscalar. The mixing angle between the CP-even scalars is called α. Therefore, there are six free parameters in this model: four Higgs masses, α and β.

Depending on how the bosons couple to up- and down-type quarks and leptons, there are different types of 2HDMs. As before, denote the two Higgs doublets as ϕ_1 and ϕ_2. The four types and their couplings are listed in Table 1.1.

	2HDM I	2HDM II	2HDM III	2HDM IV
u	ϕ_2	ϕ_2	ϕ_2	ϕ_2
d	ϕ_2	ϕ_1	ϕ_2	ϕ_1
e	ϕ_2	ϕ_2	ϕ_1	ϕ_2

Table 1.1: Higgs doublet couplings to fermions in the four types of 2HDMs [22].

At tree level, we can also compute the couplings of the neutral Higgs bosons (H, h and A) to up- and down-type quarks, leptons and gauge bosons in the four types of 2HDMs relative to the SM Higgs boson couplings as a function of α and β (Table 1.2). Note that in the scenario where $\sin^2(\beta-\alpha)=1$, for type-II 2HDM, h has the same couplings as the SM Higgs whereas H decouples from gauge bosons. In this case, H's decays to diphotons are purely fermionic. This limit is called the alignment limit, and we will present a search for this case in Chapter 9.

	2HDM I	2HDM II	2HDM III	2HDM IV
hVV	$\sin(\beta-\alpha)$	$\sin(\beta-\alpha)$	$\sin(\beta-\alpha)$	$\sin(\beta-\alpha)$
hQu	$\cos\alpha/\sin\beta$	$\cos\alpha/\sin\beta$	$\cos\alpha/\sin\beta$	$\cos\alpha/\sin\beta$
hQd	$\cos\alpha/\sin\beta$	$-\sin\alpha/\cos\beta$	$\cos\alpha/\sin\beta$	$-\sin\alpha/\cos\beta$
hLe	$\cos\alpha/\sin\beta$	$-\sin\alpha/\cos\beta$	$-\sin\alpha/\cos\beta$	$\cos\alpha/\sin\beta$
HVV	$\cos(\beta-\alpha)$	$\cos(\beta-\alpha)$	$\cos(\beta-\alpha)$	$\cos(\beta-\alpha)$
HQu	$\sin\alpha/\sin\beta$	$\sin\alpha/\sin\beta$	$\sin\alpha/\sin\beta$	$\sin\alpha/\sin\beta$
HQd	$\sin\alpha/\sin\beta$	$\cos\alpha/\cos\beta$	$\sin\alpha/\sin\beta$	$\cos\alpha/\cos\beta$
HLe	$\sin\alpha/\sin\beta$	$\cos\alpha/\cos\beta$	$\cos\alpha/\cos\beta$	$\sin\alpha/\sin\beta$
AVV	0	0	0	0
AQu	$\cot\beta$	$\cot\beta$	$\cot\beta$	$\cot\beta$
AQd	$-\cot\beta$	$\tan\beta$	$-\cot\beta$	$\tan\beta$
ALe	$-\cot\beta$	$\tan\beta$	$\tan\beta$	$-\cot\beta$

Table 1.2: Tree level couplings of neutral Higgs bosons to quarks, leptons and gauge bosons in the four types of 2HDMs relative to the SM Higgs boson couplings as a function of α and β [22].

Chapter 2

The CMS Detector

2.1 The Large Hadron Collider

The Large Hadron Collider (LHC) [23] is the largest and most powerful particle collider that has ever been built. It is a ring collider built by the European Organization for Nuclear Research (CERN), intended for pp collisions at a center-of-mass energy of 14 TeV. In 2011 the center-of-mass energy was 7 TeV whereas during the 2012 data-taking period, the center-of-mass energy reached 8 TeV. After the two-year shutdown period of 2013 and 2014, the LHC intends to restart with the full energy of 14 TeV. The collider is funded by and built with a collaboration of over 10,000 scientists and engineers from over 100 countries as well as hundreds of universities and laboratories. It lies in a tunnel 27 kilometers (17 mi) in circumference, as much as 175 meters (570 ft) beneath the Franco-Swiss border near Geneva, Switzerland. In order to keep the particles traveling in a fixed radius while being accelerated, the magnetic field of its superconducting magnets will be increased from 0.54 to over 8 Teslas[6].

There are six detector sites located around the LHC. Each of the detectors will conduct experiments and record data with its own main research purpose. Some also have similar research goals. There are four main detectors among the six: CMS ("Compact Muon Solenoid") and ATLAS ("A Toroidal LHC ApparatuS") are two general-purpose detectors

which detect and measure particles resulted from collisions. Both serve the main purposes of searching for the existence of the Higgs boson and candidates for dark matter constituents. Although the LHC is mainly intended for *pp* collisions, the program also includes short running periods (typically one month per year) of heavy-ion collisions. ALICE("A Large Ion Collider Experiment") is used to study Pb-Pb collisions. LHCb ("Large Hadron Collider beauty") is used to study *b*-physics.

2.2 The Compact Muon Solenoid

2.2.1 Overview

The analyses presented in this dissertation use data collected by the CMS detector[24]. The detector is built around a large solenoid magnet. This takes the form of a cylindrical coil of superconducting cable, cooled to -268.5 Celsius, which generates a magnetic field of 4 Tesla. CMS consists of layers of detector material that exploit the different properties of particles to measure the energy or momentum of each one. These quantities give clue to the particles' identities and properties.

The structure of the CMS is shown in Figure 2.1. The tracker is made of silicon and is used to chart particles' positions when they emit from collisions. In this way the particles' momenta are measured. Outside the tracker is the Eletromagnetic Calorimeter (ECAL) which measures the energy of photons and electrons. The ECAL was designed to have very good energy resolution (1-2%) for electrons and photons. This is critical for searches such as a Higgs boson decaying to two photons which benefits greatly from good diphoton mass resolution. The Hadron Calorimeter (HCAL) is used to measure the energy of hadrons (particles made up of quarks and anti-quarks). It is a stack of alternating brass plates and plastic scintillators. The brass plates act as absorbers to slow down particles passing through. The scintillators produce rapid light pulses as particles pass though. The light pulses are then transferred through optic fibres to photodetectors to be amplified. The amount of light in a given region is then summed up over many layers of tiles in depth

(called a "tower") and is a measure of the particle's energy. Jets, as they are mainly made up of hadrons, are detected by the HCAL. The outer part of CMS, the Muon Chamber with iron return yoke, is used to measure muons and stop all particles except muons and weakly interacting particles.

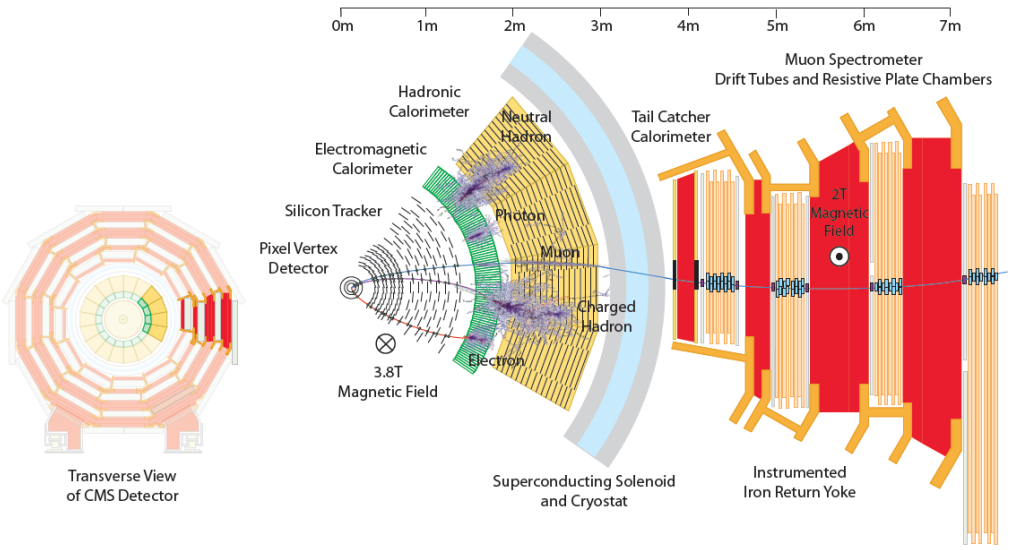

Figure 2.1: Overview of the CMS detector.

2.2.2 The Trigger System

When the LHC is running there are about one billion proton-proton interactions taking place every second. It is impossible for CMS to read out and record all these data. Furthermore, many of these events will not be interesting since they might be low-energy glancing collisions instead of head-on hard collisions. In order to select the most interesting events, triggers are employed.

The two levels of triggers at CMS are the Level 1 (L1) triggers and the High Level Triggers (HLT)[25, 27]. The L1 triggers, which are based on custom electronics, will reduce the event rate to 100kHz and the HLT triggers, which are based on commercial processors, will reduced the rate to about 100Hz. This is the maximum rate that can be read out and stored on computer disk for subsequent offline analysis.

The L1 and HLT triggers work very differently. The L1 triggers can identify basic

muon, electron, photon, jet, and missing transverse energy candidates by accessing rough segmented data from the detector and storing all the high-resolution data in pipeline memories in the front-end electronics, while the HLT trigger can access the complete data to identify particles in greater detail and accuracy.

Since the time between beam crossings at the LHC is 50 ns, the L1 trigger system must be able to accept a new event every 50 ns or less. If the L1 trigger generates an accept, the event data are assigned to a buffer for readout and processing by the HLT. Because the L1 trigger rate is limited by the speed of the detector electronics readout and the rate at which the data can be harvested by the data acquisition system, its selection criteria should utilize the most distinctive signatures of the particle objects.

The L1 trigger is comprised of several subcomponents associated with the different subdetectors: the bunch crossing timing, the L1 muon systems (CSC, DT, RPC), the L1 calorimetry (RCT, GCT) and the global trigger (GT) as shown in Figure 2.2. The GT has the ability to provide up to 128 trigger algorithms to select an event based on logical combinations of L1 objects.

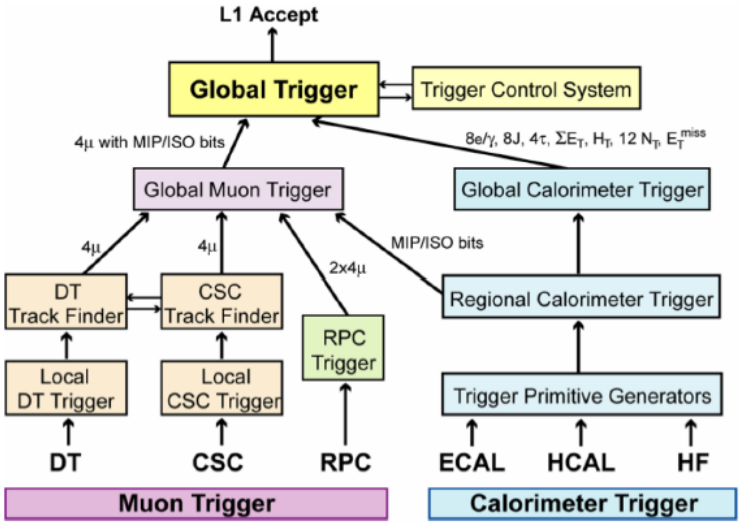

Figure 2.2: CMS L1 trigger flow chart.

On the other hand, the HLT has access to all the information used in L1 and beyond.

Much information that is not available on the time scale of the L1 decision can be accessed by the HLT. This information includes information from the tracker and the full granularity of the calorimeters. Consequently, the HLT can make further combinations and other topological calculations on the digital list of objects transmitted from L1. It is important to note that although HLT has a less stringent timing constraint than the L1 triggers, it is still important to keep the HLT processing time within a reasonable scale. Timing studies on each of the HLT modules are indispensable during the validation process of each HLT menu. Figure 2.3 shows the flow chart of the CMS L1 and HLT triggers.

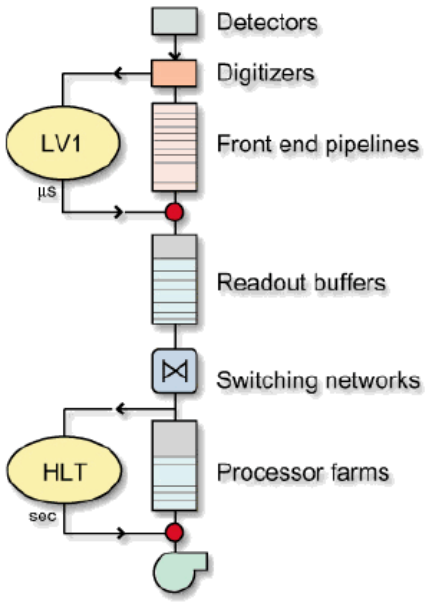

Figure 2.3: CMS trigger flow chart.

2.2.3 The Electromagnetic Calorimeter

The Electromagnetic Calorimeter [28] is able to detect and measure accurately the high energy photons from the diphoton decay of the postulated Higgs boson, thanks to the excellent energy and position resolution provided by its homogeneity and its clear, fast and radiation-tolerant crystals. It is located between the silicon tracker and the Hadron Calorimeter. It is made of 75848 lead tungstate (PbWO4) crystals (61200 in the central barrel region and

7324 in each of the two endcaps). The lead tungstate crystals are mainly made of metal, but oxygen is added to the material in order to make it highly transparent. This material scintillates when electromagnetic particles pass through it and produces light in proportion to the particles' energies. The light is collected by photodetectors and transformed into a current form that will be then transformed into other forms of signals (e.g. voltage) to be measured by subsequent parts of the detector. In this way CMS is able to determine the position and energy of an outgoing electromagnetic particle. The high density of the crystals also makes the calorimeter radiation-resistant, so that it functions well under the typical high-radiating LHC environment. These features make the ECAL a fast and accurate particle detector. Just in front of the endcap region a preshower detector is installed. Two types of photodetectors are installed in the ECAL. In the barrel region ($\mid \eta \mid \leq 1.479$) avalanche photodiodes (APDs) are used whereas in the endcap region ($1.566 \leq \mid \eta \mid \leq 3.0$) vacuum phototriodes (VPTs) are used.

APDs are made of semi-conducting silicon and applied with a strong electric field. They are able to produce in a short amount of time a great number of electrons, which results in a very high current. This feature greatly enhances the particle-detecting sensitivity in the ECAL barrel region. In the endcaps, on the other hand, the level of radiation is too high to use silicon photodiodes. Therefore here vacuum phototriodes are used instead.

Although the crystals are radiation resistant, they will still suffer loss of optical transmission under the highly radioactive environment at the LHC. These damages are monitored by the laser monitoring system installed in the ECAL [29]. By injecting pre-set laser pulses into the crystals via optical fibres, we can measure the crystal response to monitor the damage of the crystal transparency. Two laser wavelengths are used for the basic source (blue/green and IR/red). At the endcap region additional light emitting diodes (LEDs) pulser systems are used as a complement to the basic laser sources in order to monitor the damages of the VPTs. They provide additional wavelength (600nm) and allows pulsing at high rate. These monitoring systems are indispensable for the ECAL calibration and subsequently all CMS analyses that utilize measurements coming from the ECAL, for example $H \to \gamma\gamma$.

The ECAL can achieve excellent energy and position resolution for electrons and photons, which can be translated into excellent diphoton mass resolution for the $H \to \gamma\gamma$ search. The ECAL barrel energy resolution for electrons has been measured in test beams to be [30]:

$$\frac{\sigma_E}{E} = \frac{2.8\%}{\sqrt{E}} \oplus \frac{0.12}{E} \oplus 0.3\%, \tag{2.1}$$

where the three parts correspond to the stochastic, noise and constant terms, and E is in units of GeV.

The timing resolution of the ECAL is measured from data using $Z \to e^+e^-$ events by comparing the time difference between the two electron energy deposits. The measured single channel timing resolution for the energy range of electrons from Z decays is 190 ps and 280 ps in EB and EE, respectively. The position resolution is obtained from comparing the ECAL and tracker positions of low bremsstrahlung isolated electrons from W decays, which is measured to be 3(5) $\times 10^{-3}$ unites in $\Delta\eta$ for EB(EE).

Chapter 3

Data and Monte Carlo Samples

The dataset used in the analyses presented in this dissertation consists of events collected at the CMS detector with $H \to \gamma\gamma$ diphoton triggers and corresponds to an intergrated luminosity of 5.1 fb^{-1} at 7 TeV (2011) and 19.6 fb^{-1} at 8 TeV (2012).

The Monte Carlo (MC) samples used in the analyses for signal modeling, training of the MVA discriminants and data/MC comparison studies are fully simulated using GEANT [31]. The simulated events include detector and pile-up (number of independent collision events per bunch crossing) effects , and are reweighed to reproduce the expected pile-up distrubutions in data. Figure 3.1 shows the distribution of number of vertices for data and reweighed MC events.

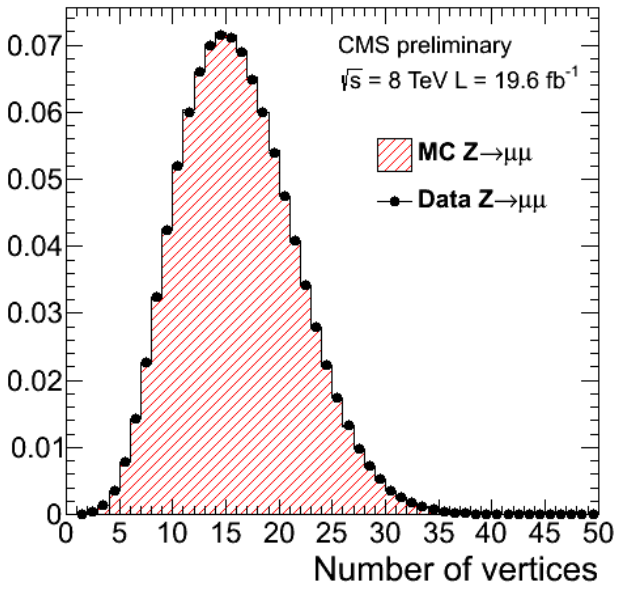

Figure 3.1: Distribution of the number of reconstructed vertices for $Z \to \mu^+\mu^-$ events in data (black dots) and pile-up reweighed MC events (hashed histogram).

Chapter 4

Trigger

4.1 Introduction

Every collision event at CMS needs to go through a series of triggers to be decided whether to be kept or not. There are two levels of triggers at CMS - the Level 1 Triggers (L1) and the High Level Triggers (HLT), as discussed in Chapter 2. The event passes through the L1 first, which uses only very basic and coarse local calorimeter or muon detector information for the decision and therefore is ideal for fast processing. The synchronous processing time for L1 is about 3 μs. Then the event passes through the HLT, which uses more complex and higher resolution information to recreate the entire event in order to look for more specific physics signature. The average processing time of the HLT is around 40 ms. For the $H \to \gamma\gamma$ analysis, the central information resides in the ECAL, and therefore the triggers which we are interested in will make decisions based on ECAL information (for example, trigger tower energy sums). The HLT paths used for the analysis are seeded from electron/photon(e/γ)-related L1 triggers. If and only if these L1 triggers are fired will the HLT make a further decision about whether to keep the full event information for the offline analysis (conditional reconstruction). After an event passes the L1 and HLT, we can then apply to it more customized offline cuts for the analysis.

The whole suite of the triggers used is called the trigger menu. When the LHC luminosity

is relatively low, we can afford to have triggers with looser requirements while staying within the rate budget. As the LHC luminosity increases, we can no longer sustain some of the triggers and would have to cyclically update the trigger menu in order to stay within the assigned rate while at the same time making sure that the triggers are highly efficient with respect to the $H \to \gamma\gamma$ signal.

4.2 Overview of $H \to \gamma\gamma$ L1 and HLT Triggers

Every $H \to \gamma\gamma$ diphoton HLT path is required to be seeded from an L1 e/γ trigger object. The L1 seeds for the $H \to \gamma\gamma$ di-photon triggers have evolved in time with the increase of LHC luminosity. We will mainly focus on the L1 seeding performance in 2012. The full L1 seeding record and performance for the 2011 data-taking period can be found in [34].

The HLT paths can be categorized into two types, one with E_T cuts of 26/18 GeV (on the lead/sublead photon) and the other with E_T cuts of 36/22 GeV. Each 26/18 path is required to be initiated by L1_DoubleEG13_7 (two L1 e/γ candidates, with minimum E_T of 13/7 GeV), whereas each 36/22 path is required to be initiated by L1_SingleEG22 (one L1 e/γ candidate with minimum E_T of 22 GeV).

Once the L1-seeding requirement has been satisfied, ECAL clusters are formed in the vicinity of the L1 seed(s). ECAL information is unpacked only from the readout units overlapping with a rectangle centered on an L1 candidate with a size $\Delta\eta \times \Delta\phi = 0.25 \times 0.4$ to save processor time in the HLT. The resulting cluster should have a position matching the L1 candidate, a transverse energy satisfying the requirements of the given L1 cut and deposit little energy in the hadron calorimeter (HCAL) region just behind it. For the 26/18 paths, we require the presence of at least two such clusters. Then, among these clusters, we require that at least two pass the relevant HLT cuts. For the single-seeded 36/22 paths, we require only one such cluster. Once this requirement is satisfied, one then tries to reconstruct another HLT candidate by unpacking the rest of the ECAL information.

The HLT cuts can be grouped into three categories: common, isolation plus calorimeter identification(Iso + CaloId), and R_9 cuts. The variable R_9 is defined as the ratio between

the energy of the 3×3 crystals around the most energetic crystal and the energy of the whole supercluster. Good photon candidates should have R_9 values close to one. This variable was introduced to recover signal-like events which would have been cut by the CaloId + Iso paths, thus enhancing the overall trigger efficiency. The variables used in the HLT include the following:

- Variables used in both paths:

  E_T of the lead/sublead photons

  The di-photon invariant mass $M_{\gamma\gamma}$

  H/E

- Variables used only in CaloId + Iso paths:

  $\sigma_{i\eta i\eta}$

  ECAL isolation

  HCAL isolation

  Track isolation

- Variables used only in R_9 paths:

  R_9

For a detailed description of these variables and the evolution of their corresponding cut values with the increase of instantaneous luminosity, please refer to [35].

Any photon that passes the general cuts and either of the Iso+CaloId or the R_9 cuts is considered a "good" photon. Therefore, the general trigger strategy is to keep all possible good photon pairs using the "OR" triggers:

HLT_Photon26_R9Id85_OR_CaloId10_Iso50_Photon18_R9Id85_OR_CaloId10_Iso50_Mass* and

HLT_Photon36_R9Id85_OR_CaloId10_Iso50_Photon22_R9Id85_OR_CaloId10_Iso50.

Note that in 2011, instead of having the compact "OR" triggers, we had four equivalent separate paths (double CaloId + Iso, double R_9, CaloId + Iso-R_9 and R_9-CaloId + Iso). Studies have been performed to verify that not only each of these two OR triggers can reproduce the collective results one would obtain using four separate triggers with corre-

sponding E_T and $M_{\gamma\gamma}$ requirements, but also the four individual paths can be extracted and reconstructed from the OR triggers using saved trigger objects.

The full evolution, design and emulation studies of the L1 and HLT paths for $H \to \gamma\gamma$ can be found in [35].

4.3 Trigger Efficiency Measurement Using Monte Carlo and $Z \to e^+e^-$ Data

In order to validate a trigger, knowing that the trigger rate stays within budget is not enough. One also needs to ensure that the trigger efficiency stays high. The HLT efficiency is defined as:

$$\text{HLT Efficiency} = \frac{\#\text{ of events passing the HLT and the offline analysis cut}}{\#\text{ of events passing the offline analysis cut}}. \quad (4.1)$$

If the efficiency is low, it means that the trigger will cut out a significant amount of desirable events. Considering that the number of $H \to \gamma\gamma$ signal events will be very limited compared to background, it is very important to keep the efficiency close to unity. Trigger efficiency measurements are performed on $H \to \gamma\gamma$ Monte Carlo events and with the tag and probe method (T&P) [36] on $Z \to e^+e^-$ data.

Efficiency studies with MC signal events are straightforward. We use $H \to \gamma\gamma$ samples with the latest pileup condition, apply the full standard offline cut for photons, then simply count the events that pass the HLT paths. The efficiency computed using MC stays over 99.5% throughout the whole data-taking period.

However, efficiency studies with MC are not enough because differences exist between MC simulation and real data. To cover this effect, T&P studies on $Z \to e^+e^-$ data are also carried out. The data sample is obtained as follows:

- From DoubleElectron Primary Dataset, select events which pass the loosely prescaled path

  HLT_Ele32_CaloIdT_CaloIsoT_TrkIdT_TrkIsoT_SC17_Mass50. Since this path requires

only one electron passing the tight HLT cuts, the other electron which is required to pass only the very loose SC17 filter, is suitable for our measurement.

- We require at least two offline photons to be matched to the HLT electron and the HLT supercluster leg, respectively. The two offline photons are required to have an invariant mass compatible with the Z peak (between 70 GeV and 110 GeV), and to pass an offline p_T cut of 30 GeV and 22.5 GeV, respectively.

- We require further that the event passes the event pre-selection cuts and has diphoton MVA value > -0.05, which is the offline event selection for the MVA analysis (see Chapter 6).

- The photon matched to the HLT electron leg is also required to be matched to an L1 e/γ isolated object with $E_T > 22$ GeV (requirement compatible with the L1-seeding of HLT_Ele32_CaloIdT_CaloIsoT_TrkIdT_TrkIsoT_SC17_Mass50). Then, we can label this photon as TAG and the other one as PROBE, and perform various efficiency calculations.

To account for the fact that electrons and photons have different R_9 distributions, each electron pair used for the trigger efficiency measurement has been reweighted so that the R_9 distribution of the associated superclusters matches that of photons according to the $H \to \gamma\gamma$ MC. The net effect is an increasing of the measured efficiency due to the migration of events towards higher R_9 values.

For events that have passed the MVA analysis offline cuts (preselection and diphoton MVA > -0.05), we found the HLT efficiency of the OR of the two triggers mentioned above to be 99.68±0.03%. The relevant L1 efficiencies are listed in Table 4.3. Similar efficiency is found for the cut-based analysis selection (see Chapter 6).

	L1_DoubleEG_13_7	L1_SingleEG_22
MVA > 0.05	99.75±0.01%	97.14±0.02%

Table 4.1: L1 efficiencies for events passing diphoton MVA output > -0.05.

The efficiencies of the L1 and HLT paths with respect to reconstructed photon p_T, η and number of vertices are also obtained using the $Z \to e^+e^-$ tag and probe method and are shown in Figure 4.1 to 4.7.

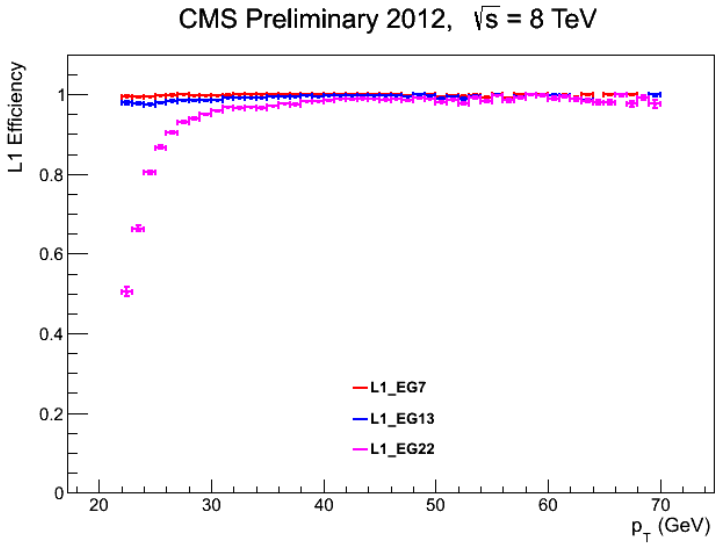

Figure 4.1: L1 efficiency as a function of reconstructed photon p_T.

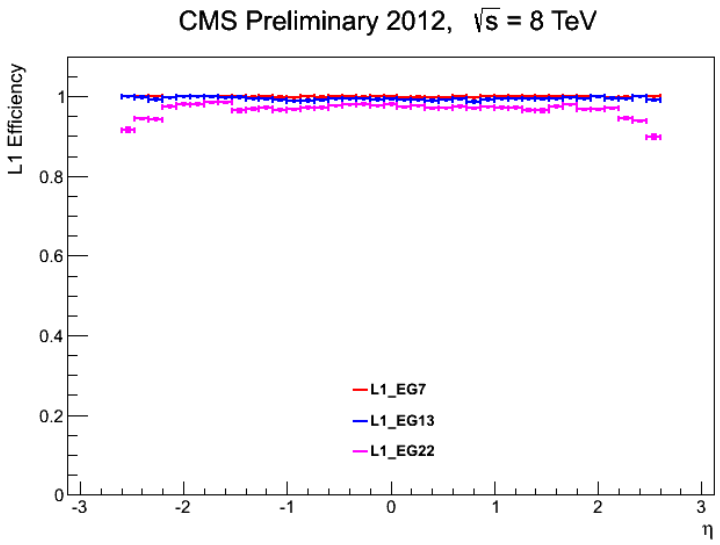

Figure 4.2: L1 efficiency as a function of reconstructed photon η.

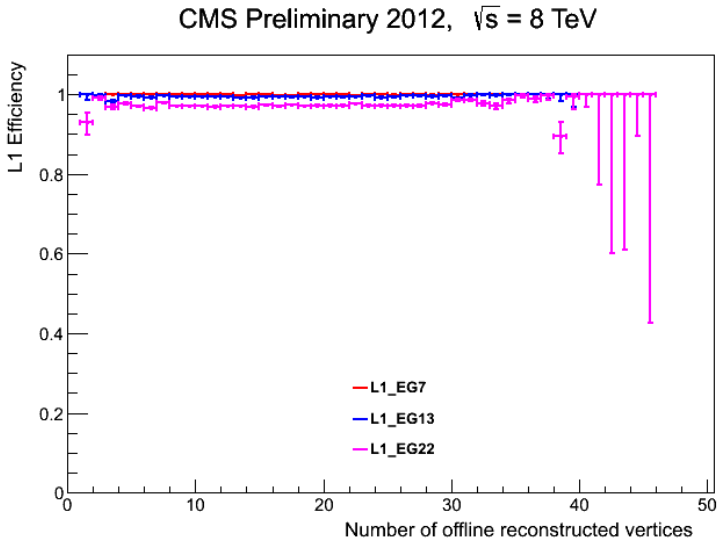

Figure 4.3: L1 efficiency as a function of number of reconstructed vertices.

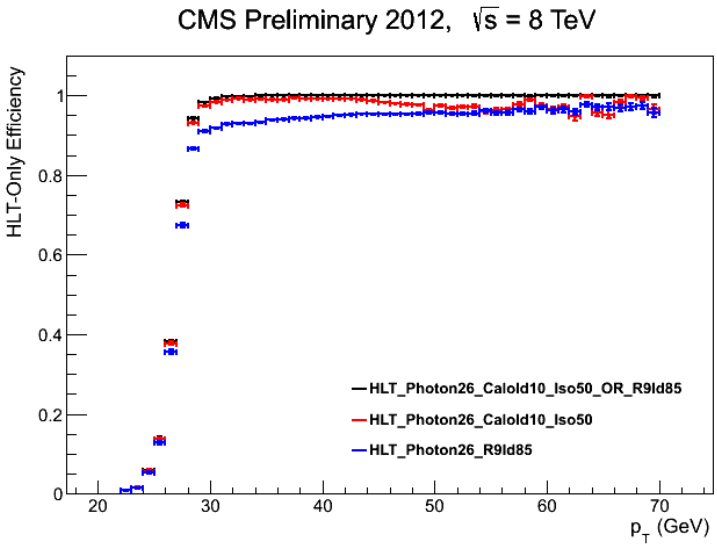

Figure 4.4: HLT efficiency as a function of reconstructed photon p_T for the HLT leg with $E_T = 26$ GeV cut.

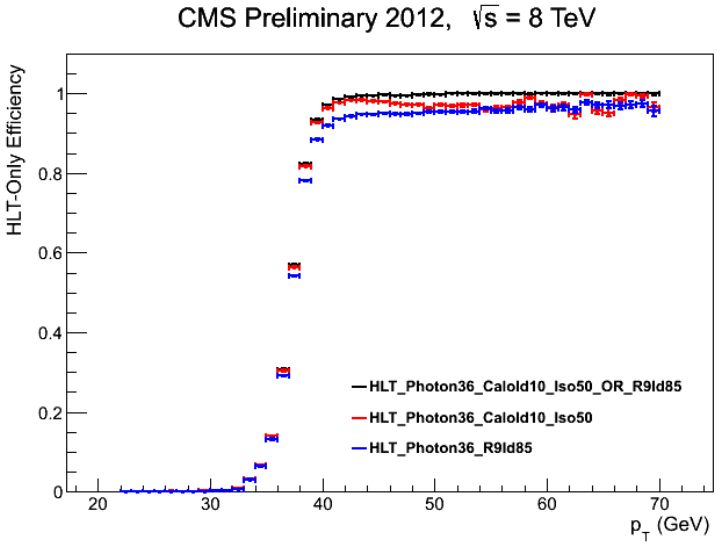

Figure 4.5: HLT efficiency as a function of reconstructed photon p_T for the HLT leg with $E_T = 36$ GeV cut.

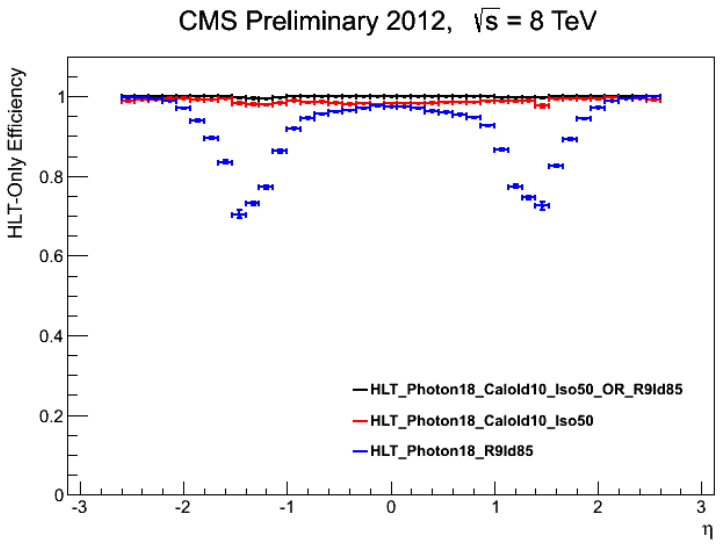

Figure 4.6: HLT efficiency as a function of reconstructed photon η.

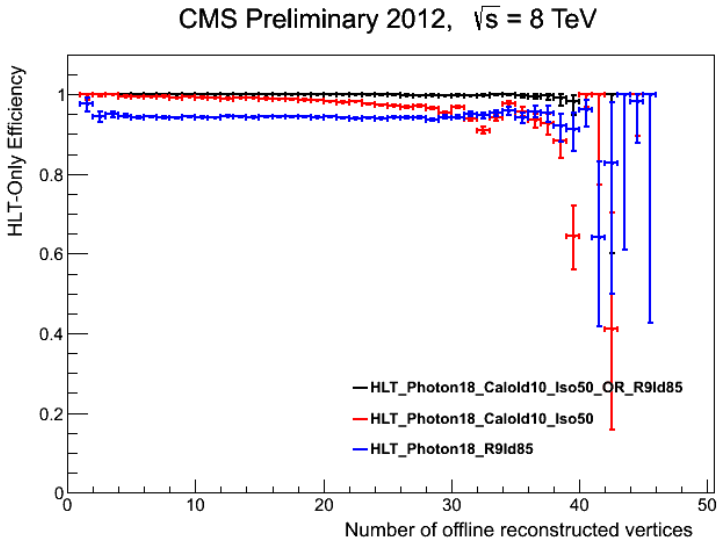

Figure 4.7: HLT efficiency as a function of number of reconstructed vertices.

Chapter 5

Photon Reconstruction and Energy Correction

5.1 Photon Reconstruction

Electron and photon showers deposit their energy in several crystals in the ECAL [28, 37]. Approximately 94% of the incident energy of a single electron or photon is contained in 3×3 crystals, and 97% in 5×5 crystals.

The presence of material in front of the calorimeter results in bremsstrahlung and photon conversions. Because of the strong magnetic field, the energy deposited in the ECAL is spread in ϕ. The spread energy is clustered by building a cluster of clusters, called a supercluster, which is extended in ϕ.

Photon candidates are reconstructed from superclusters [38]. In the ECAL barrel region, superclusters are formed from strips in η that have a width of five crystals, centered at the most energetic crystal, called the seed, and have a variable width in ϕ. This is called the hybrid clustering algorithm. In the endcap region, the superclusters are formed using the island algorithm. Matrices of 5×5 crystals around the most energetic crystals are merged if they lie within a narrow ϕ range.

The complete sequence for ECAL reconstruction is illustrated in Figure 5.1. The first

step is to perform local reconstruction of ECAL reconstruction hits (RecHits). This is followed by hybrid clustering or island clustering. The next step is to apply an energy scale correction to the peak of the reconstructed distribution of E_T. The correction is a parametric function of the number of crystals in the seed of the supercluster. Additional energy deposited in the preshower ($|\eta| \geq 1.65$) is added as the final step in the ECAL reconstruction procedure.

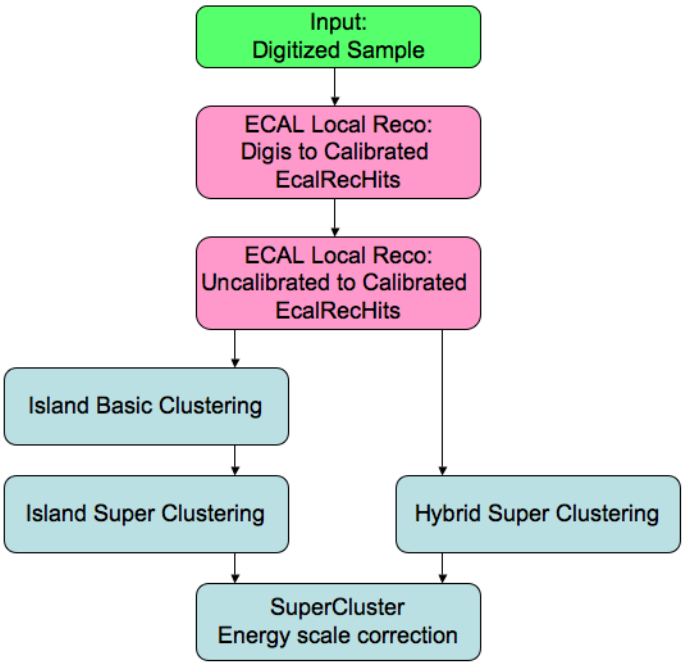

Figure 5.1: CMS ECAL reconstruction flow chart.

About half of the photons convert in the material in front of the ECAL. Conversion track pairs are reconstructed from a combination of Gaussian-Sum-Filter (GSF) electron tracks and ECAL-seeded tracks fit to a common vertex and then matched to the photon candidate.

5.2 Photon Energy Reconstruction

5.2.1 Photon Energy Reconstruction Overview

Photon energy is computed starting from the raw energy deposited in the ECAL crystals [26, 30]. The energy in a supercluster can be expressed as:

$$E_{e,\gamma} = F_{e,\gamma} \times [G \times \sum_i S_i(t) \times C_i \times A_i + E_{ES}] \tag{5.1}$$

where the sum is over all the crystals i in the supercluster. The various terms in the equation are:

- $F_{e,\gamma}$ is the energy correction necessary to take into account η- and ϕ-dependent geometry and material effects as well as differences between photons and electrons.
- G is the ADC-to-GeV conversion factor (measured separately for EB, EE and ES).
- The time-dependent S_i's are the corrections for changes in response due to irradiation.
- The C_i's are the per-channel inter-calibration constants.
- The A_i's are the amplitudes of the signal reconstructed with the ADC counts and their weights.
- E_{ES} is the energy from the preshower for regions of $|\eta| \geq 1.65$.

Due to various detector effects, the crystal energies are calibrated in order to obtain the most correct values and best energy resolution. Changes in the crystal transparency due to irradiation ($S_i(t)$) are monitored and corrected for using lights of different wavelengths injected from the laser and LED systems, as discussed in Chapter 2. The single-channel response of the ECAL (C_i) is calibrated using the ϕ-symmetry method, the invariant mass distribution of photon pairs from π^0 and η decays, and the momentum distribution of isolated electrons from $W \to e\nu$ and $Z \to e^+e^-$ decays. Figure 5.2 shows the reconstructed invariant mass distribution from $Z \to e^+e^-$ decays in steps of calibration procedures.

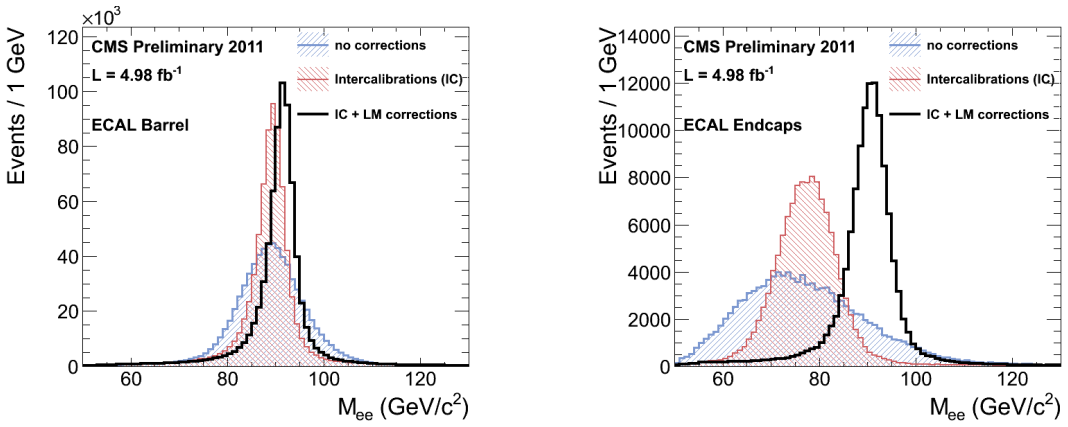

(a) calibrationEB. (b) calibrationEE.

Figure 5.2: Reconstructed invariant mass from $Z \to e^+e^-$ decays in steps of calibration procedures: inter-calibrations (IC) and laser monitoring corrections (LM).

The correction factor $F_{e,\gamma}$ is derived from Monte Carlo to account for energy containment effects using a multivariate regression technique based on a Boosted Decision Tree (BDT) [39]. The regression is trained on photons in MC samples starting from the raw energy and using the MC truth energy as the target. A second BDT provides an event-by-event energy uncertainty estimate. It is trained on an independent sample of MC photons, starting from the correction predicted by the first BDT and the true deviation to generator-level energy. Figure 5.3 shows the comparison between the dielectron invariant mass from $Z \to e^+e^-$ decays using energy constructed by applying a fix clustering of 5×5 crystals, the standard supercluster energy and the regression-corrected supercluser energy.

The absolute energy scale G and the residual time-dependent drifts in the response are corrected using data and MC events from $Z \to e^+e^-$ decays. This part will be discussed in detail in the following sections.

5.2.2 Energy Scale Correction for Data

After applying calibration factors and per-photon energy corrections from regression, energy scales corrections for data and additional smearings for MC are derived to resolve the remaining discrepancies between data and MC. The energy scale corrections are derived by

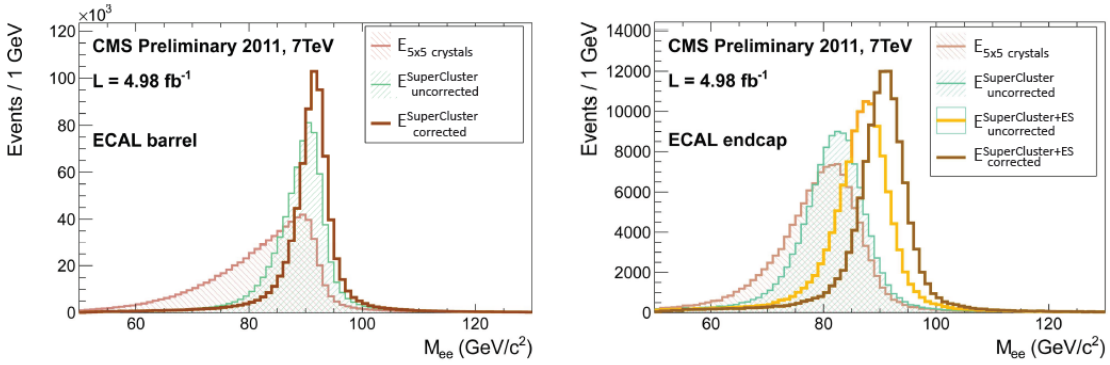

Figure 5.3: Reconstructed invariant mass for electrons from $Z \to e^+e^-$ events, using energy constructed by applying a fix clustering of 5×5 crystals, the standard supercluster energy and the regression-corrected supercluser energy.

comparing the dielectron invariant mass line shapes from $Z \to e^+e^-$ events in data and MC (Z fit method), over run ranges, 4 η, and 2 R_9 categories. The dielectron invariant mass distribution is fit with a Breit-Wigner shape convoluted with a Crystal Ball function. For both MC and data, the Breit-Wigner parameters are fixed to the Particle Data Group values. For data, the tail parameters of the Crystal Ball function are fixed to be the fitted values from MC. Then the remaining free parameters for both data and MC are Δm and σ_{CB}. Eventually, for each category, the per-electron scale correction is obtained by:

$$\Delta P = \frac{\Delta m_{data} - \Delta m_{MC}}{m_Z}. \tag{5.2}$$

Figure 5.4 shows the EB/EE energy scales before and after run-dependent corrections across 2012 run periods.

5.2.3 Energy Resolution Correction for MC

The energy resolution in MC tends to be over-optimistic and needs to be corrected with respect to data. This is achieved by deriving additional MC smearing factors using a likelihood-based method (smearing method). For each η- and R_9-based category, define 2 parameters ($\Delta\sigma$, ΔP). Next, construct dielectron invariant mass distributions from $Z \to$

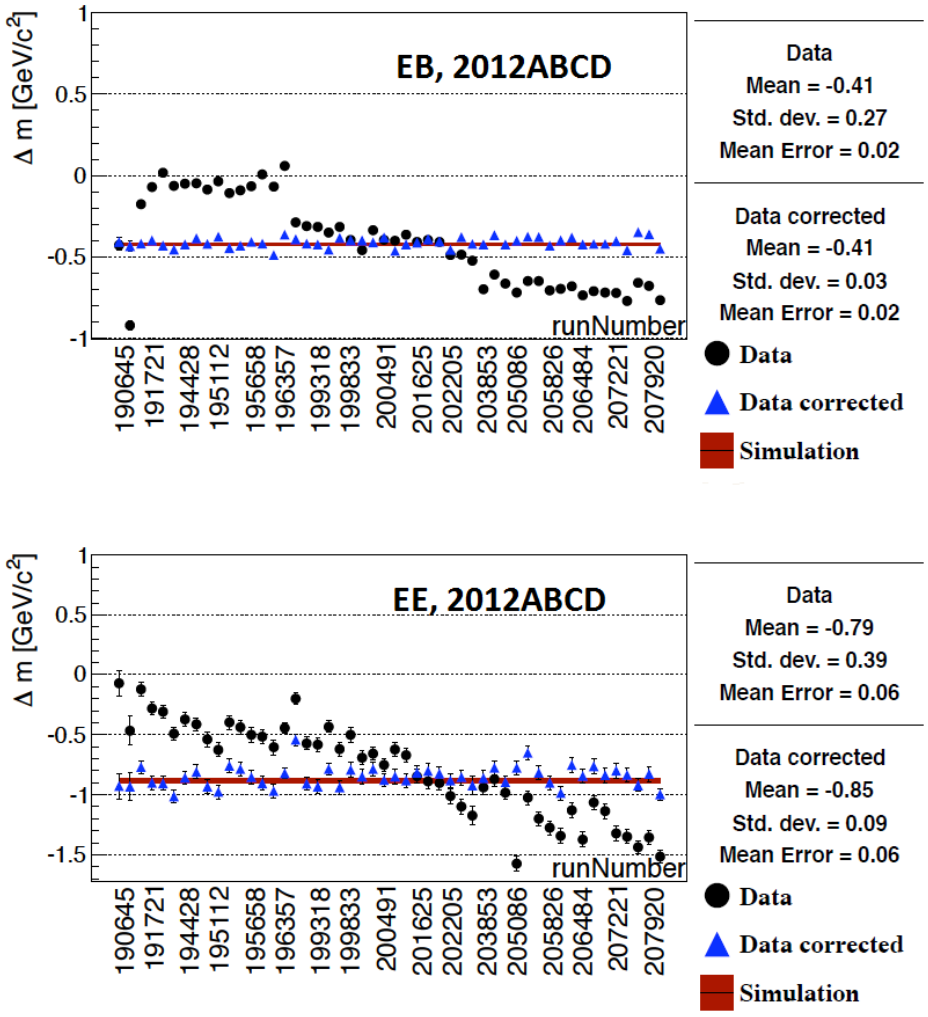

Figure 5.4: EB/EE energy scales before and after run-dependent corrections using the Z fit method across 2012 run periods.

e^+e^- events for each possible electron category pair for data. The same distributions are then constructed for MC, but smeared by $E_{smeared} = E\times$ Gaus $(1 + \Delta P, \Delta\sigma)$. The per-category ($\Delta\sigma$, ΔP) are extracted by the configuration that gives the best data/MC match using a likelihood function. The additional smearing factors are obtained by:

$$add.\ smearing = \sqrt{2 \times ((\frac{\sigma_{CB,data}}{peak_{CB,data}})^2 - (\frac{\sigma_{CB,MC}}{peak_{CB,MC}})^2)}. \tag{5.3}$$

Figure 5.5 shows the data and MC comparisions before and after applying the additional MC smearings for two categories.

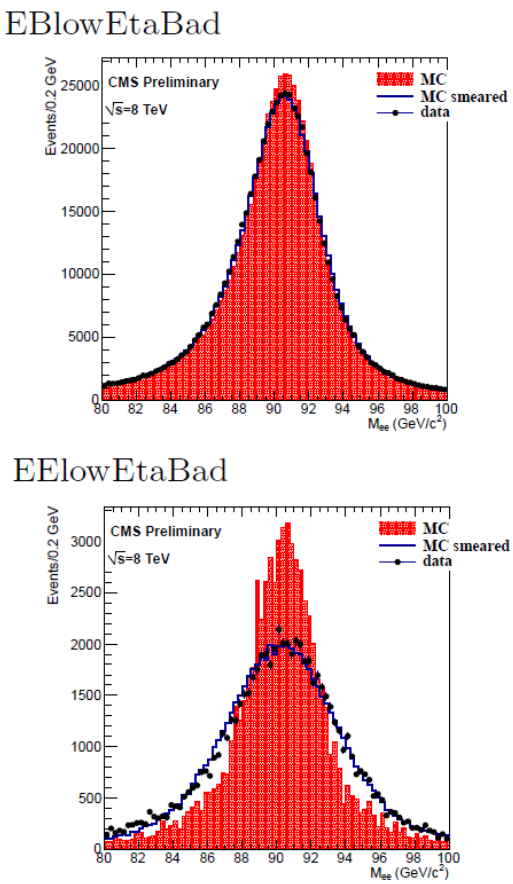

Figure 5.5: Data and MC comparisions before and after applying the additional MC smearings using 2012 data for two categories.

Chapter 6

Search Strategy Overview

6.1 Search Signature

We search for a localized excess of diphoton events that constitute a narrow peak over a smoothly falling background. The search range is from 110 GeV to 150 GeV. The width of the peak is dominated by the instrumental resolution as the SM prediction of the Higgs natural width is 4 MeV. The background consists of a large irreducible component originated from QCD production of two prompt photons via Box($gg \to \gamma\gamma$) and Born($q\bar{q} \to \gamma\gamma$) processes, and an additional reducible component of events where at least one of the two photon candidates comes from misidentification of jet fragments. A powerful photon identification technique will be able to separate signal events from reducible background events, whereas the main handle on discriminating irreducible background lies in the event kinematics variables.

We will mainly discuss two analyses in this dissertation: an MVA-based analysis and a cut-based analysis [40, 41]. They were carried out side-by-side in 2012. The MVA analysis has been the main analysis of the $H \to \gamma\gamma$ group, whereas the cut-based analysis is more straightforward and serves as a cross-check on the MVA analysis. Detailed descriptions on the following analysis ingredients can be found in [42].

6.2 Event Pre-Selection

A loose set of pre-selection cuts are applied in both the MVA and cut-based analyses, listed in Tables 6.1 and 6.2. They are designed to match the cuts in the HLT triggers.

	Barrel		Endcap	
R9	HoE	CovIEtaIEta	HoE	CovIEtaIEta
≤ 0.9	< 0.075	< 0.014	< 0.075	< 0.034
> 0.9	< 0.082	< 0.014	< 0.075	< 0.034

Table 6.1: Preselection cuts (part one).

	Both Barrel and Endcap		
R9	EtCorrHcalIso	EtCorrTrkIso	ChargedPFIso
≤ 0.9	< 4 GeV	< 4 GeV	< 4 GeV
> 0.9	< 50 GeV	< 50 GeV	< 4 GeV

Table 6.2: Preselection cuts (part two).

6.3 Vertex Identification

In addition to the photon energy resolution, the diphoton mass resolution also depends on the resolution in measuring the opening angle between the two photons. Consequently the ability to determine the correct diphoton vertex is essential to the search. Since photons do not leave ionization signals in the tracker, the diphoton vertex is identified indirectly using the kinematic properties of the diphoton system and its correlations with the kinematic properties of the recoiling tracks.

The method used to select the best primary vertex candidate is based on a multivariate approach exploiting the kinematic properties of the vertex tracks and their correlation with the diphoton kinematics, and adding the tracker information for converted photons. Inputs to the vertex BDT include the sum, the degree of balance and the degree of asymmetry of the transverse momenta of the two photons. A second BDT provides the estimation of an event-by-event probability for the correct vertex assignment as an input to the final

diphoton MVA for event selection and categorization.

6.4 Photon Identification

6.4.1 Photon ID MVA

For the MVA-based analysis, a BDT classifier is employed to distinguish prompt photons from fakes, mainly jets from $pp \to \gamma$ + jet and $pp \to$ jet + jet. The output BDT value of each photon is also used as a input variable for the diphoton MVA for event selection and categorization. Input variables for the photon ID MVA include shower topology variables, photon isolation variables based on the particle flow algorithm [32], the event energy density ρ [33] and the supercluster η. Figure 6.1 shows the photon ID MVA output for MC signal and background, for ECAL barrel and endcap separately. As a very loose pre-selection, a cut of -0.2 on the photon ID MVA output is applied to both photons.

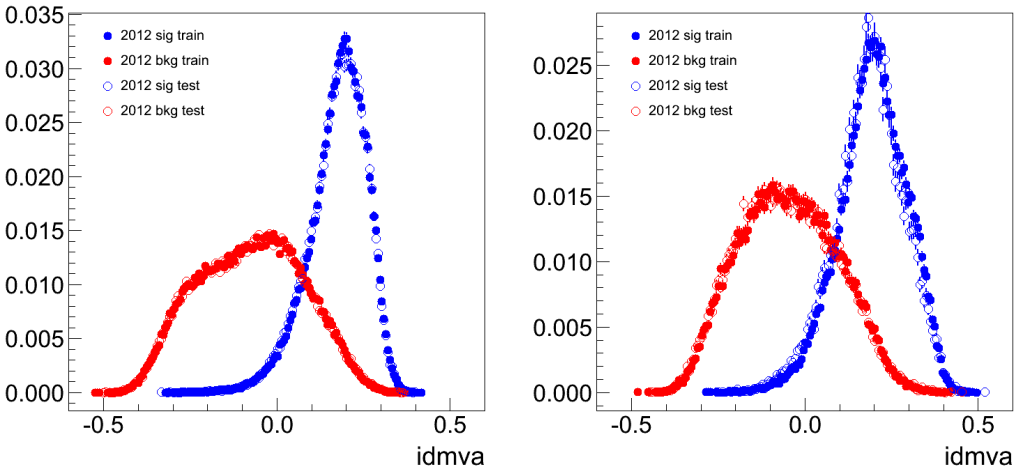

Figure 6.1: Photon ID MVA output for barrel (left) and endcap (right).

6.4.2 Cut-Based Photon ID

For the cut-based analysis, photons are categorized into four categories based on their η (EB or EE) and R_9 (greater or less than 0.94) values. For each category, a set of cut values,

optimized separately for each category, are applied to select events. These four categories have significantly differing levels of background and mass resolution and their use provides increased sensitivity. The list of variables used and their corresponding cut values are listed in Table 6.3.

	barrel		endcap	
	$R9 > 0.94$	$R9 < 0.94$	$R9 > 0.94$	$R9 < 0.94$
PF isolation sum, chosen vertex (GeV)	6	4.7	5.6	3.6
PF isolation sum worst vertex (GeV)	10	6.5	5.6	4.4
Charged PF isolation sum (GeV)	3.8	2.5	3.1	2.2
$\sigma_{i\eta i\eta}$	0.0108	0.0102	0.028	0.028
H/E	0.082	0.075	0.075	0.063
$R9$	0.94	0.298	0.94	0.24

Table 6.3: Photon ID selection cut values for the cut-based analysis. The cuts are applied to both photons and are optimized to select an overall sample of photons with the best S/B for a particular signal photon efficiency.

6.5 Event Selection and Categorization

In general, events are categorized into tagged and untagged categories. The tagged categories target specific production modes:

1. Muon tag (VH)
2. Electron tag (VH)
3. Dijet tag (VBF)
4. MET tag (VH).

The specific selection for these tagged categories for the MVA and cut-based analyses can be found in [42]. By taking advantage of the high signal/background ratio, they increase the analysis sensitivity significantly. All remaining events after the tagged categories selection are then passed on to the untagged cateogories selection.

6.5.1 Untagged Event Categorization for the Cut-Based Analysis

The cut-based analysis categorizes events based on the η and R_9 of the two photons (Table 6.3). Besides the photon ID cuts, the only cut on the event is on $p_{\mathrm{T}}/\mathrm{m}_{\gamma\gamma}$, where $\mathrm{m}_{\gamma\gamma}$ is the candidate diphoton invariant mass. The "sliding cut" has been fixed to be 1/3 and 1/4 respectively on the leading and subleading photon. This means a cut of 40 GeV (leading) and 30 GeV (subleading) for a candidate invariant mass of 120 GeV.

6.5.2 Untagged Event Selection and Categorization for the MVA Analysis

The MVA analysis requires the same "sliding cut" on the photon $p_{\mathrm{T}}/\mathrm{m}_{\gamma\gamma}$ as the cut-based analysis (1/3 for the leading photon and 1/4 for the subleading photon). However, instead of categorizing using photon R_9 and η as in the cut-based analysis, events are categorized using a BDT classifier, such that the high-performance classes are predominately populated by events with good resolution and/or high signal-background ratio. The following variables are used as inputs to the BDT:

1. the relative transverse momenta of both photons, $p_{\mathrm{T}}^{1(2)}/m_{\gamma\gamma}$,
2. the pseudo-rapidities of both photons, $\eta^{1(2)}$,
3. the cosine of the angle between the two photons in the transverse plane, $\cos(\phi_1 - \phi_2)$,
4. the photon identification BDT output value for both photons,
5. the per-event relative mass resolution estimate assuming the mass has been constructed using the correct primary vertex,
6. the per-event relative mass resolution estimate assuming the mass has been constructed using the incorrect primary vertex,
7. The per-event probability that the correct primary vertex has been used to reconstruct the diphoton mass, computed from a linear fit to the event-level vertex selection MVA as described in Section 6.3.

Then, four cut boundaries for categorizing events were determined by scanning the BDT output value and optimizing for the best expected exclusion limit.

6.6 Signal and Background Modeling

The MVA analysis and the cut-based analysis share the same procedure for modeling signal and background distributions.

The strategy for modeling the signal shape is to fit sums of Gaussians to MC events per production mode and per class at each available MC mass point (5 GeV separation), after applying corrections determined from data/MC comparisons of $Z \to e^+e^-$ and $Z \to \mu^+\mu^-\gamma$ events. The full signal model is then defined by a linear interpolation of each fit parameter between the fitted mass values. The signal model is slightly modified for the measurement of the Higgs decay width, by convoluting the Gaussians with a Breit-Wigner function, which will be discussed in Chapter 8.

The modeling of the background is fully parametric and data driven. This is done by fitting Bernstein polynomials to data per event class, where the orders of the polynomials were adjusted to keep the estimated potential bias less than 1/5 of the statistical error. A Bernstein polynomial of order N is defined as:

$$N\mathrm{Ber}(x) := \sum_{i=0}^{N} \beta_i b_{(i,N)}, \quad \text{with} \quad b_{(i,N)} := \left(\begin{array}{c} N \\ i \end{array} \right) x^i (1-x)^{N-i} \quad . \tag{6.1}$$

This model serves as fully-differential prediction of the mean expected diphoton mass distribution in the background-only hypothesis and is needed in the statistical procedure that determines exclusion limits or the significance of an observation.

The expected signal and background yields, as well as the signal model specifics are listed in Table 6.4.

Expected signal and estimated background										
Event classes		SM Higgs boson expected signal (m_H=125 GeV)							Background	
		Total	ggH	VBF	VH	ttH	σ_{eff} (GeV)	FWHM/2.35 (GeV)	$m_{\gamma\gamma}$=125 GeV (ev./GeV)	
7 TeV 5.1 fb^{-1}	Untagged 0	3.2	61.4%	16.8%	18.7%	3.1%	1.21	1.14	3.3	± 0.4
	Untagged 1	16.3	87.6%	6.2%	5.6%	0.5%	1.26	1.08	37.5	± 1.3
	Untagged 2	21.5	91.3%	4.4%	3.9%	0.3%	1.59	1.32	74.8	± 1.9
	Untagged 3	32.8	91.3%	4.4%	4.1%	0.2%	2.47	2.07	193.6	± 3.0
	Dijet tag	2.9	26.8%	72.5%	0.6%	–	1.73	1.37	1.7	± 0.2
8 TeV 19.6 fb^{-1}	Untagged 0	17.0	72.9%	11.6%	12.9%	2.6%	1.36	1.27	22.1	± 0.5
	Untagged 1	37.8	83.5%	8.4%	7.1%	1.0%	1.50	1.39	94.3	± 1.0
	Untagged 2	150.2	91.6%	4.5%	3.6%	0.4%	1.77	1.54	570.5	± 2.6
	Untagged 3	159.9	92.5%	3.9%	3.3%	0.3%	2.61	2.14	1060.9	± 3.5
	Dijet tight	9.2	20.7%	78.9%	0.3%	0.1%	1.79	1.50	3.4	± 0.2
	Dijet loose	11.5	47.0%	50.9%	1.7%	0.5%	1.87	1.60	12.4	± 0.4
	Muon tag	1.4	0.0%	0.2%	79.0%	20.8%	1.85	1.52	0.7	± 0.1
	Electron tag	0.9	1.1%	0.4%	78.7%	19.8%	1.88	1.54	0.7	± 0.1
	$E_{\text{T}}^{\text{miss}}$ tag	1.7	22.0%	2.6%	63.7%	11.7%	1.79	1.64	1.8	± 0.1

Table 6.4: Expected number of SM Higgs boson events (m_H=125 GeV) and estimated background (at $m_{\gamma\gamma}$=125 GeV) for all event classes of the 7 and 8 TeV datasets for the MVA analysis. The composition of the SM Higgs boson signal in terms of the production processes and its mass resolution are also given.

6.7 Systematic Uncertainties

The systematic uncertainties affecting the signal are listed in Table 6.5. Detailed descriptions on each item and the methods used to estimate them can be found in [41].

6.8 Statistical Treatment

The SM Higgs boson hypothesis is tested against the background-only hypothesis by performing a simultaneous fit to the diphoton invariant mass distributions in the various event classes under each of the two hypotheses. The 95% confidence level exclusion limits on the signal strength modifier (μ) are evaluated using a modified frequentist approach, CL_s, taking the profile likelihood ratio as a test statistic [43, 44, 45].

The local p-value quantifies the probability for the background to produce a fluctuation as large as the observed one or larger, and assumes that the relative signal strength between the event classes follows the MC signal model for the SM Higgs boson.

Measurements of the SM Higgs boson mass are performed using a profiled likelihood scan, and the 68% and 95% confidence level regions are extracted accordingly. The upper limit on the SM Higgs boson decay width is set with the Feldman-Cousins method [49].

Sources of systematic uncertainty		**Uncertainty**	
Per photon		Barrel	Endcap
Energy resolution ($\Delta\sigma/E_{MC}$)	$R_9 > 0.94$ (low η, high η)	0.23%, 0.72%	0.93%, 0.36%
	$R_9 < 0.94$ (low η, high η)	0.25%, 0.60%	0.33%, 0.54%
Energy scale ($(E_{data} - E_{MC})/E_{MC}$)	$R_9 > 0.94$ (low η, high η)	0.20%, 0.71%	0.88%, 0.12%
	$R_9 < 0.94$ (low η, high η)	0.20%, 0.51%	0.18%, 0.12%
Photon identification efficiency		1.0%	2.6%
Cut-based			
$R_9 > 0.94$ efficiency (results in class migration)		4.0%	6.5%
MVA analyses			
Photon identification BDT		±0.01 (shape shift)	
(Effect of up to 4.3% event class migration.)			
Photon energy resolution BDT		±10% (shape scaling)	
(Effect of up to 8.1% event class migration.)			
Per event			
Integrated luminosity		4.4%	
Vertex finding efficiency		0.2%	
Trigger efficiency		1.0%	
Global energy scale		0.47%	
Dijet selection			
Dijet-tagging efficiency	VBF process	10%	
	Gluon-gluon fusion process	30%	
(Effect of up to 15% event migration among dijet classes.)			
Muon selection			
Muon identification efficiency		1.0%	
Electron selection			
Electron identification efficiency		1.0%	
$E_{\mathrm{T}}^{\mathbf{miss}}$ **selection**			
$E_{\mathrm{T}}^{\mathrm{miss}}$ cut efficiency	Gluon-gluon fusion	15%	
	Vector boson fusion	15%	
	Associated production with W/Z	4%	
	Associated production with $t\bar{t}$	4%	
Production cross sections		Scale	PDF
Gluon-gluon fusion		+7.6% -8.2%	+7.6% -7.0%
Vector boson fusion		+0.3% -0.8%	+2.6% -2.8%
Associated production with W/Z		+2.1% -1.8%	4.2%
Associated production with $t\bar{t}$		+4.1% -9.4%	8.0%

Table 6.5: Separate sources of systematic uncertainties accounted for in the analysis of the 8 TeV data set.

Chapter 7

Search Results Using the Combined 7 TeV and 8 TeV Datasets

In this chapter we present results from searches for a Standard Model Higgs boson decaying into two photons performed with the MVA analysis and the cut-based analysis, using the combined 7 TeV and 8 TeV datasets [41], with a quick reference to the discovery results presented on July 4th, 2012 [46, 47].

7.1 Search Results with the MVA Analysis Using the Combined 2011 and 2012 Datasets

Figure 7.1 shows the diphoton invariant mass distribution for all event classes for 7 TeV and 8 TeV combined, together with the sum of background model fits for the 14 event classes (5 for 7 TeV and 9 for 8 TeV).

The 95% exclusion limits for a SM Higgs decaying to two photons are shown in Figure 7.2. The observed results exclude a SM Higgs boson at 95% CL in the mass ranges 110.0–123.0 GeV and 128.0–149.0 GeV.

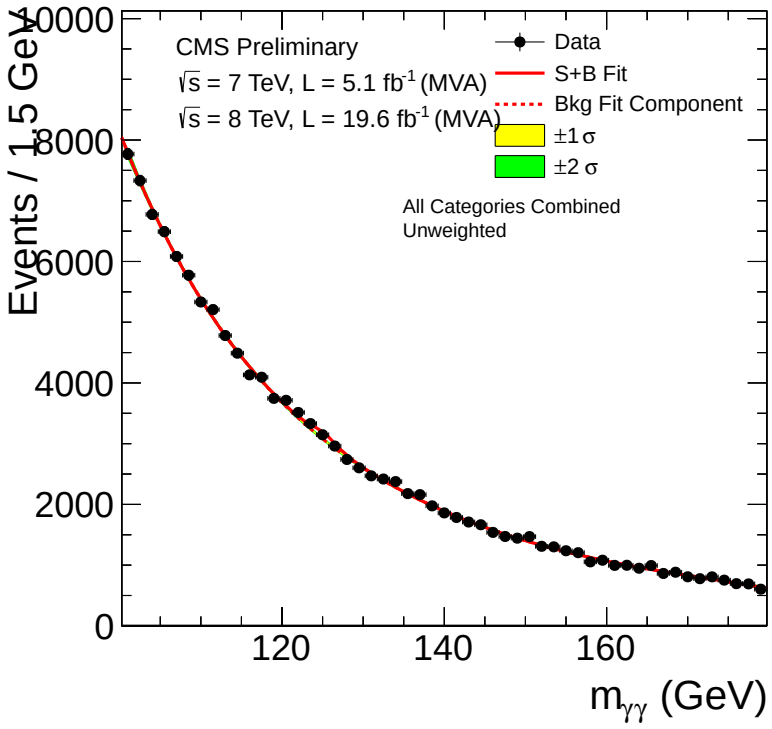

Figure 7.1: Sum of background model fits for the 14 event classes overlaid on the combined 7 TeV and 8 TeV datasets.

The probability that the observed distribution arises from the background only hypothesis (the p-value), computed as a profile likelihood ratio with respect to a SM-like Higgs with floating overall cross-section, is shown in Figure 7.8. The most significant excess occurs for a hypothesis mass of 125.0 GeV, with a local significance of 3.2 σ (expected 4.2 σ).

Figure 7.4 shows the best fit signal strength as a function of the hypothesized Higgs boson mass. For a Higgs boson mass hypothesis of 125.0 GeV, the best fit signal strength is $0.78^{+0.28}_{-0.26}$ times the SM Higgs boson cross-section.

Figure 7.5 (left) shows the 2D 68% confidence level region for the signal strength μ and the mass of the observed particle. Figure 7.5 (right) shows the scan of the negative log-likelihood as a function of the hypothesized mass, evaluated using statistical uncertainties only (blue dashed line), and using statistical plus systematic uncertainties (black line). The mass of the observed boson is measured to be $125.4 \pm 0.5(stat.) \pm 0.6(syst.)$ GeV. From

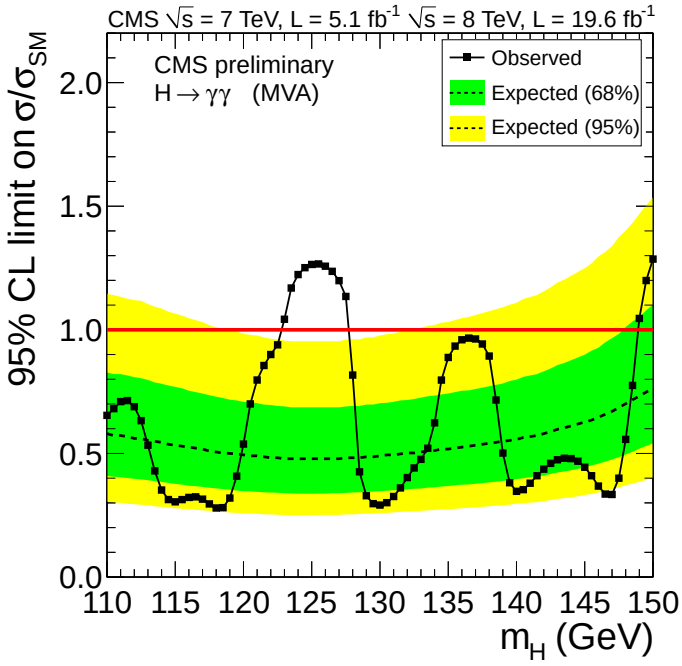

Figure 7.2: Observed and expected exclusion limits (95% CL) on the cross-section as a ratio to the expected SM cross-section in the asymptotic CLs approximation, for the combined 7 TeV and 8 TeV datasets, for the MVA analysis.

Figure 1.6, we see that data strongly suggests that Higgs boson mass skirts the metastability border.

7.2 Search Results with the Cut-Based Analysis Using the Combined 2011 and 2012 Datasets

Figure 7.10 shows the diphoton invariant mass distribution for all event classes for 7 TeV and 8 TeV combined, together with the sum of background model fits for the 14 event classes.

The 95% exclusion limits for a SM Higgs decaying to two photons are shown in Figure 7.7. The observed results exclude a SM Higgs at 95% CL in the mass ranges 110.0–121.5 GeV and 128.5–149.0 GeV.

The p-value of the background hypothesis is shown in Figure 7.8. The most significant

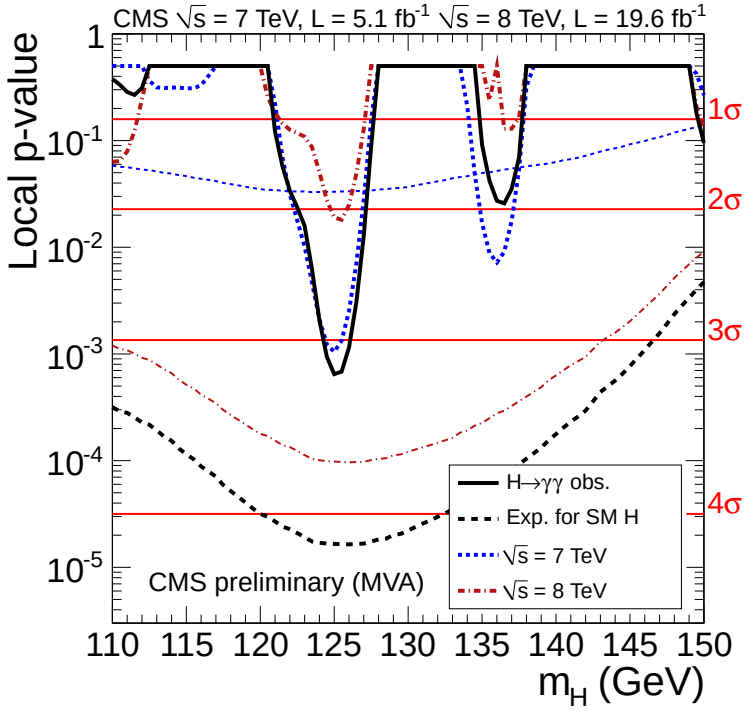

Figure 7.3: Observed and median expected local p-values for a Standard Model Higgs boson as a function of hypothesized Higgs mass, for the combined 7 TeV and 8 TeV datasets, for the MVA analysis.

excess occurs for a hypothesis mass of 124.5 GeV, with a local significance of 3.9σ, compared to a median expected p-value of 3.5σ.

Figure 7.9 shows the best fit signal strength as a function of the hypothesized Higgs boson mass. For a Higgs boson mass hypothesis of 124.5 GeV, the best fit signal strength is $1.11^{+0.32}_{-0.30}$ times the SM Higgs boson cross-section.

7.3 Search Results Presented on July 4th, 2012

For the sake of completeness, we include here also the results presented at the CERN seminar on July 4th, 2012, as it marks the discovery of a SM Higgs-like boson. The datasets used in the results presented in this section include 5.1 fb^{-1} from 7 TeV and 5.3 fb^{-1} from 8 TeV. The equivalent result presented by the ATLAS collaboration can be found in [48].

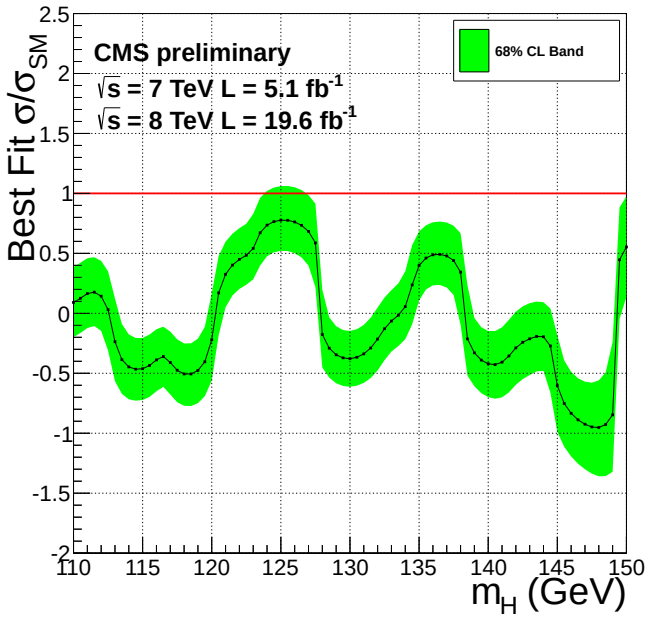

Figure 7.4: Best fit of σ/σ_{SM} as a function of the hypothesized Higgs boson mass, for the combined 7 TeV and 8 TeV datasets, for the MVA analysis.

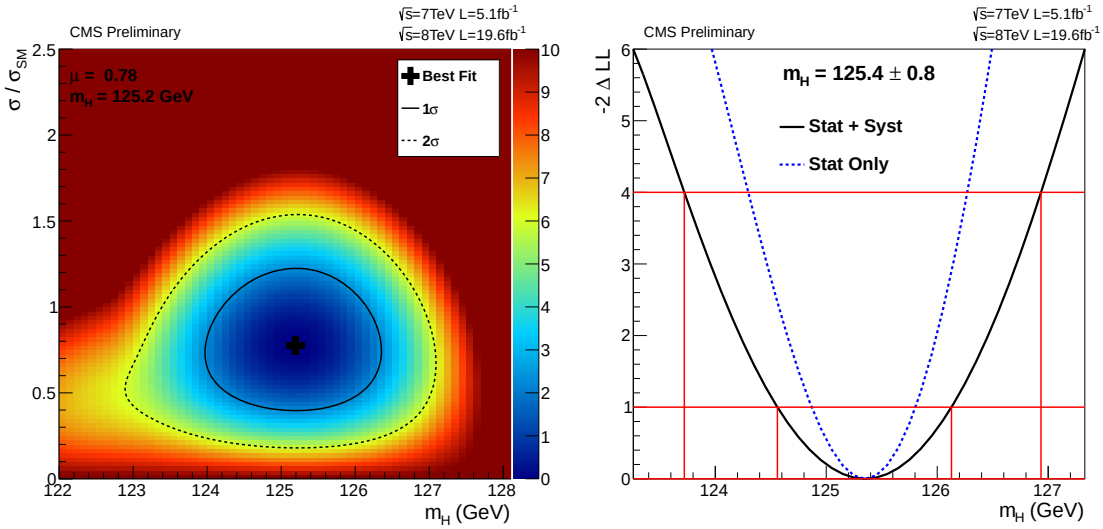

Figure 7.5: (left) The 2D 68% confidence level region for the signal strength modifier μ and the mass of the observed particle. (right) The scan of the negative log-likelihood as a function of the hypothesized mass, evaluated using statistical uncertainties only (blue dashed line), and using statistical plus systematic uncertainties (black line).

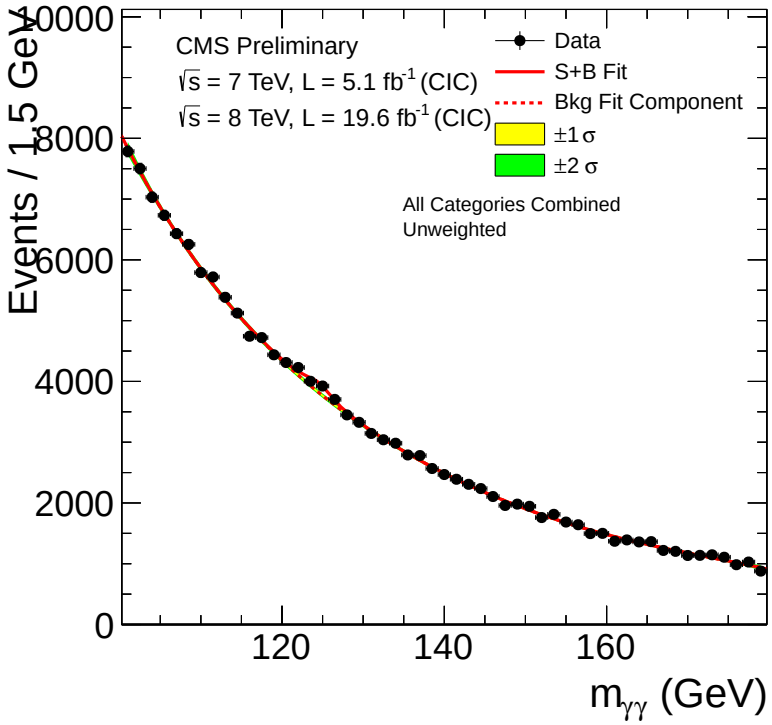

Figure 7.6: Sum of background model fits for the 14 event classes overlaid on the combined 7 TeV and 8 TeV datasets.

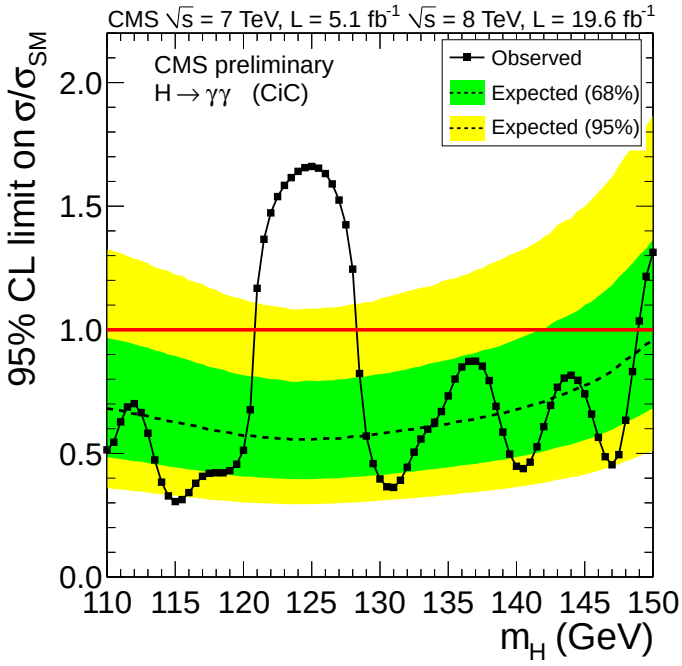

Figure 7.7: Expected exclusion limits (95% CL) on the cross-section as a ratio to the expected SM cross-section in the asymptotic CLs approximation, for the combined 7 TeV and 8 TeV datasets.

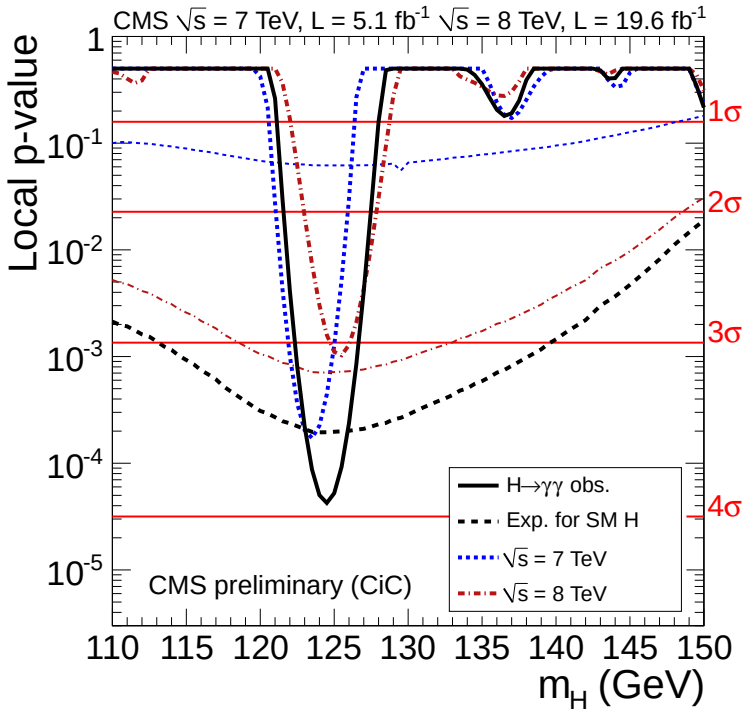

Figure 7.8: Observed and median expected p-values from a Standard Model Higgs boson across the full mass range, for the combined 7 TeV and 8 TeV datasets.

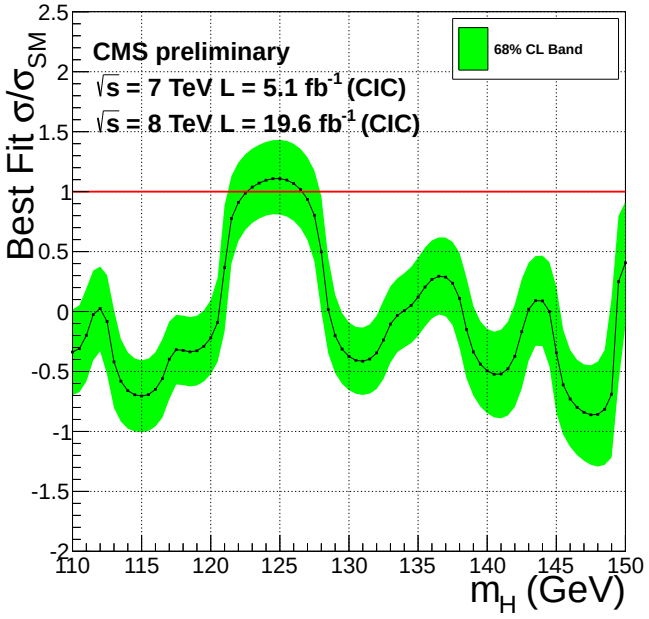

Figure 7.9: Best fit of σ/σ_{SM} as a function of the hypothesized Higgs boson mass, for the combined 7 TeV and 8 TeV datasets.

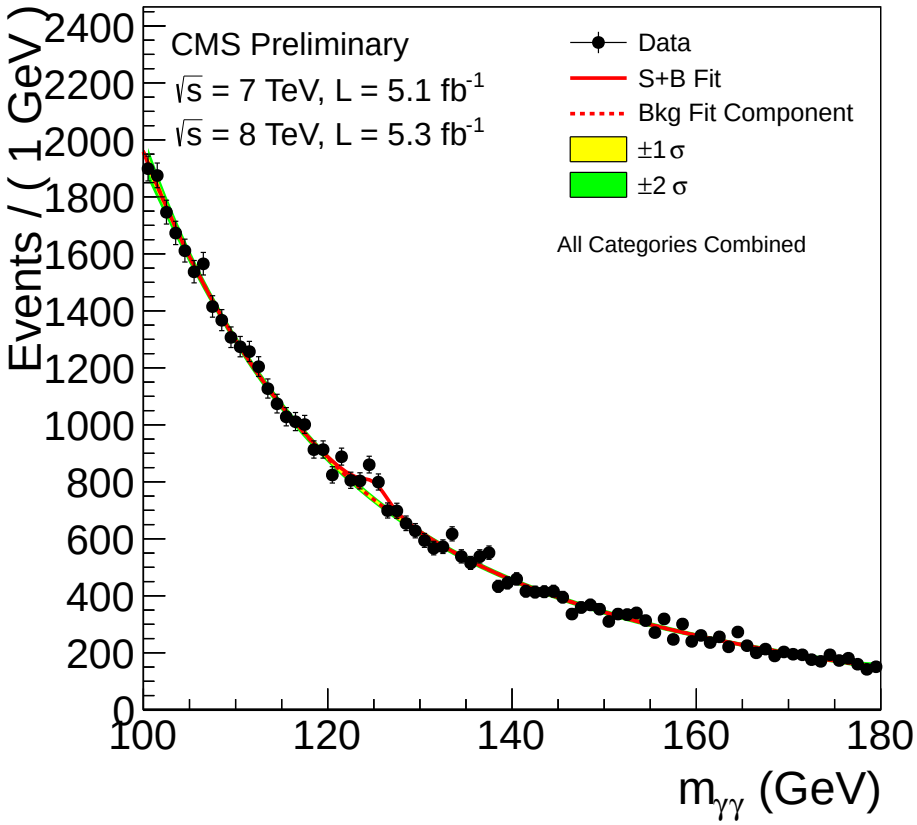

Figure 7.10: Sum of background model fits for the six classes overlaid on the combined data, for the 7 TeV dataset from 2011 combined with 5.3 fb^{-1} 8 TeV dataset from 2012.

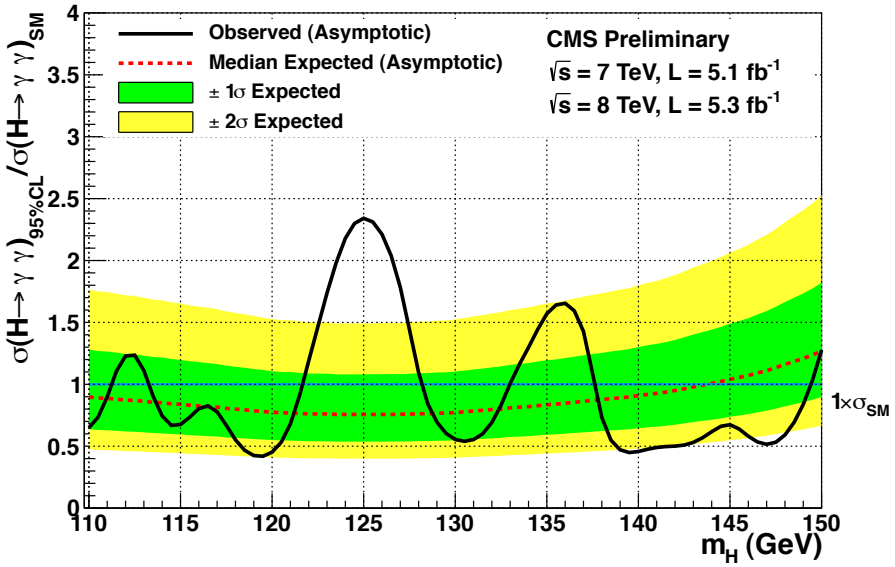

Figure 7.11: Expected exclusion limits (95% CL) on the cross section as a ratio to the expected SM cross section in the asymptotic CLs approximation, for the 7 TeV dataset from 2011 combined with 5.3 fb^{-1} 8 TeV dataset from 2012.

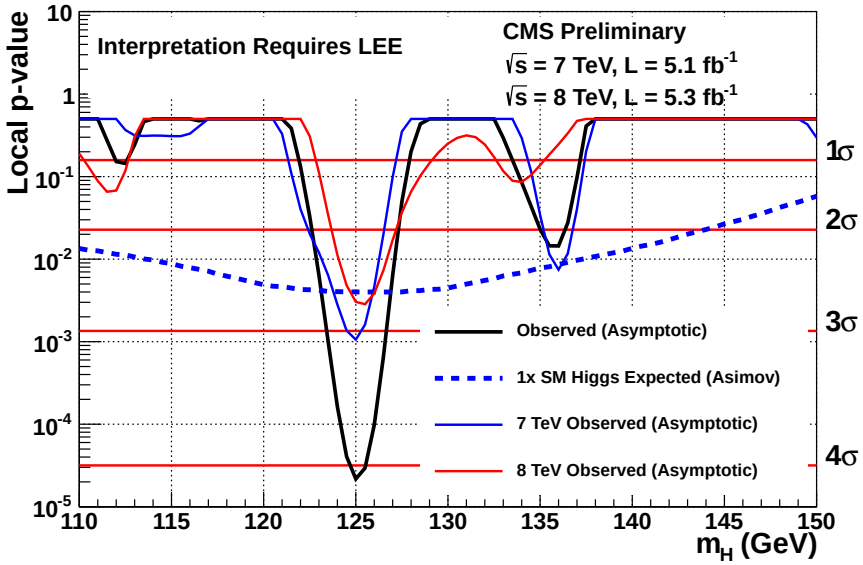

Figure 7.12: Median expected p-values from a Standard Model Higgs boson across the full mass range, for the 7 TeV dataset from 2011, for 5.3 fb^{-1} 8 TeV dataset from 2012, and for the two datasets combined.

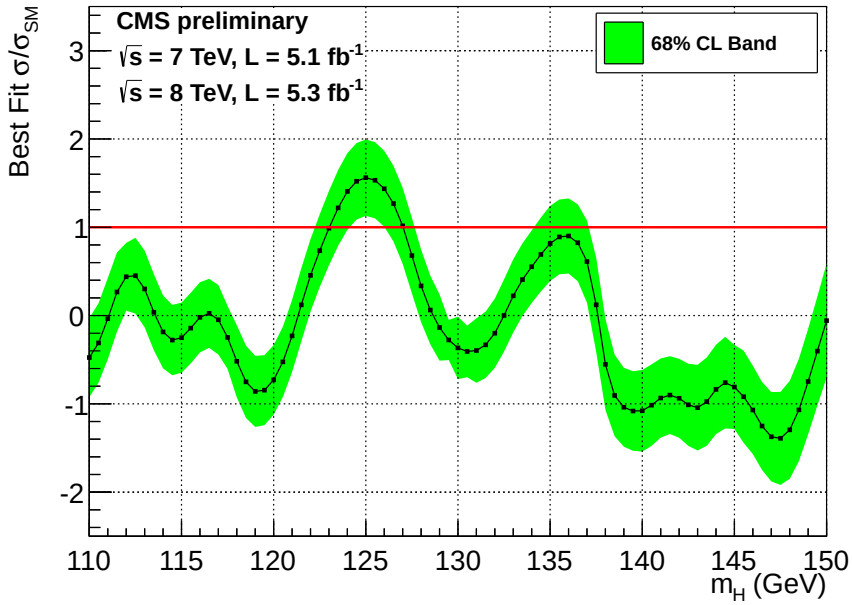

Figure 7.13: Best fit of σ/σ_{SM} as a function of the hypothesized Higgs mass, for the 7 TeV dataset from 2011 combined with 5.3 fb^{-1} 8 TeV dataset from 2012.

Chapter 8

Measurement of the Higgs Natural Width

Using the same event selection and categorization as the MVA analysis, it is possible to set a limit on the Higgs natural width by changing the signal model.

The signal model for the main analysis is parameterized as a sum of Gaussians and is defined continuously for any value of 110 GeV $\leq m_H \leq$ 150 GeV. This can be extended in a simple fashion to allow for an additional free parameter, the natural width of the observed boson, Γ_H, by convoluting the signal shape with a Breit-Wigner function which has a mean of m_H and a width of Γ_H. The convolution of a Breit-Wigner fuction with a Gaussian is called a Voigtian.

To ensure smooth interpolation between the MC mass points, we adopt a procedure of fitting all the mass points simultaneously and requiring the fit parameters to be smooth functions of MC mass values. Figure 8.1 shows the signal model for all categories combined. The signal models for the individual categories are shown in Figure 8.2.

The profiled likelihood estimator on the width of the observed boson is defined as:

$$q_w = -2 \ln \frac{\mathcal{L}(\text{obs}|w, \hat{\theta}_w)}{\mathcal{L}(\text{obs}|\hat{w}, \hat{\theta})} = -2\Delta \ln \mathcal{L}(w)$$

where w is the width parameter, "obs"' indicates the observed data, $\hat{w}$ and $\hat{\theta}$ are the values

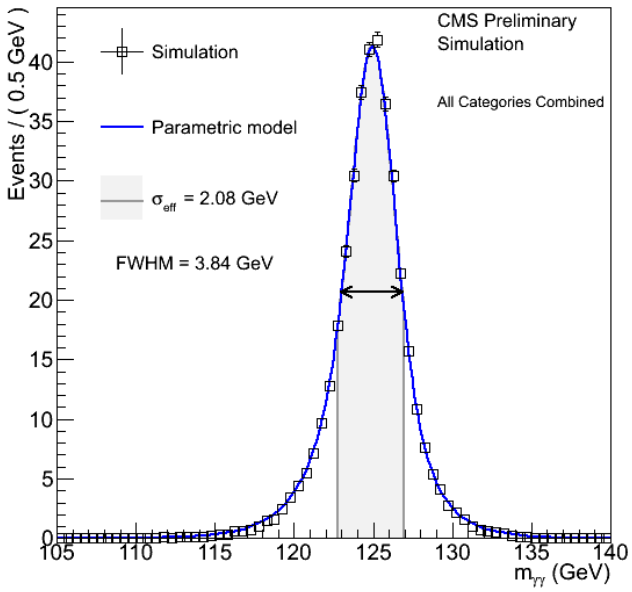

Figure 8.1: Signal model for all event classes in 125 GeV Higgs Monte Carlo events. The black points are the Monte Carlo events and the blue lines are the corresponding parametric signal model. Also shown is the effective σ value and the corresponding interval.

of the width and nuisance parameters at the global maximum of the likelihood $\mathcal{L}$. $\hat{\theta}_w$ is the set of nuisance parameter values which maximize the likelihood $\mathcal{L}$ for a fixed value of the width w.

Since the best-fit value of the Higgs natural width is close to the zero boundary (since its theoretical value is 4 MeV), the 95% CL upper limit on the decay width of the Higgs boson is evaluated using the Feldman-Cousins method [49], instead of using the usual negative log-likelihood curve.

Figure 8.3 shows $-2\Delta \ln \mathcal{L}$ as function of the width parameter for the combined 7 TeV and 8 TeV datasets for the MVA analysis. The observed (expected) upper limit on the width is 6.9 (5.9) GeV/c^2 at 95% confidence level.

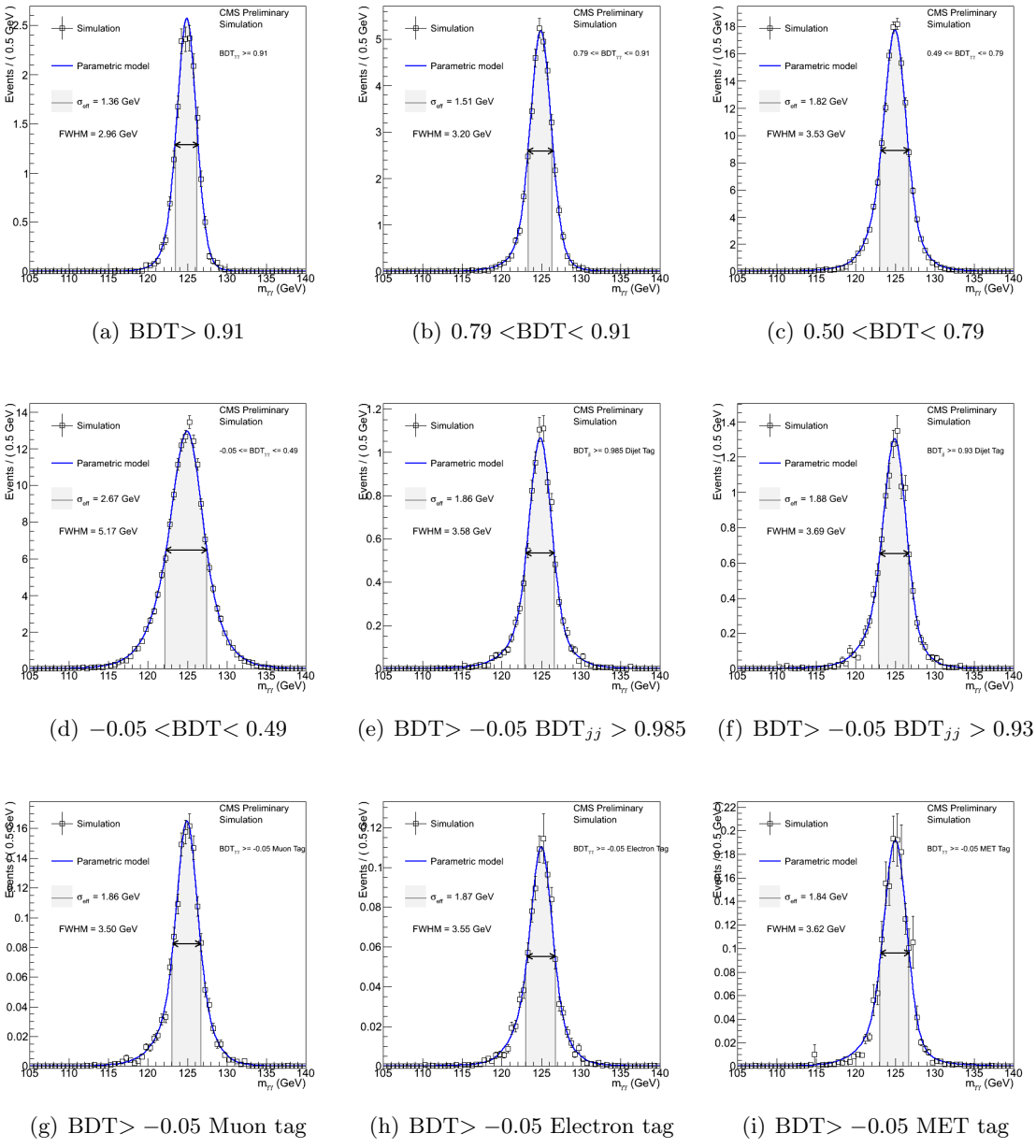

(a) BDT> 0.91 (b) 0.79 <BDT< 0.91 (c) 0.50 <BDT< 0.79

(d) −0.05 <BDT< 0.49 (e) BDT> −0.05 $\mathrm{BDT}_{jj} > 0.985$ (f) BDT> −0.05 $\mathrm{BDT}_{jj} > 0.93$

(g) BDT> −0.05 Muon tag (h) BDT> −0.05 Electron tag (i) BDT> −0.05 MET tag

Figure 8.2: Signal models for the 9 categories in 125 GeV Higgs Monte Carlo events. The black points are the Monte Carlo events and the blue lines are the corresponding parametric signal models. Also shown are the effective σ values and the corresponding intervals.

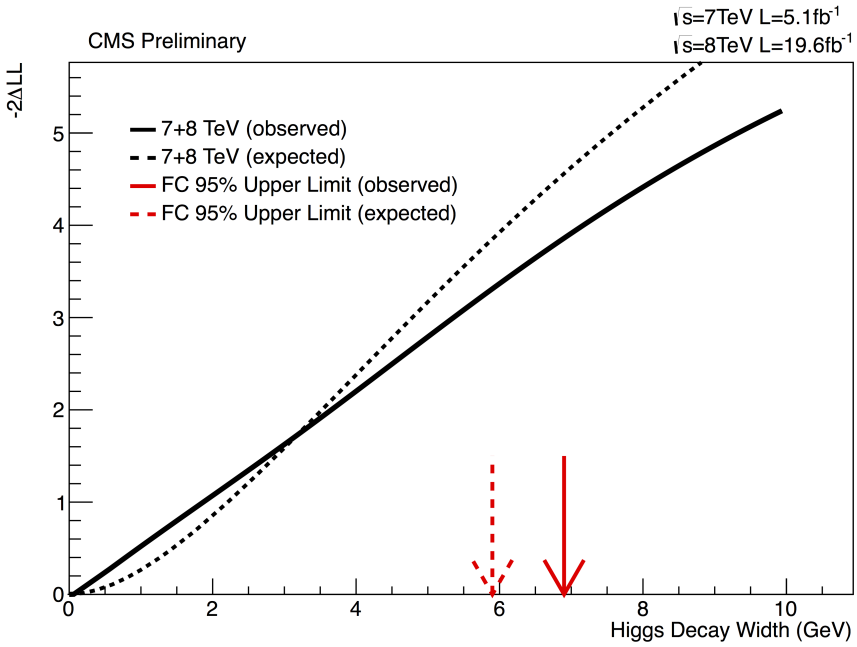

Figure 8.3: Evolution of the logarithm of the likelihood ratio as function of the decay width for the MVA analysis, 7 TeV and 8 TeV datasets combined. The observed (expected) upper limit on the width is 6.9 (5.9) GeV/c^2 at 95% confidence level, calculated using the Feldman-Cousins method.

Chapter 9

Searches for an Additional State

As discussed in Chapter 1, states which share decay modes and comparable in mass are strongly motivated in multi-Higgs sectors. For example, within a 2HDM, the CP-even h, H and the CP-odd A may all decay into two photons. Depending on the admixture, the relative rates of two states decaying into the diphoton final state can be comparable.

Near mass degeneracy and larger mass splitting are predicted in these models. To search for a pair of Higgs bosons within the current analysis range can already be a powerful test of these theories. As a first step, we consider the second Higgs boson as SM-like, that is, we use the same event selection and signal model as the MVA analysis.

In order to separately test the case where the masses of the two states are very close to each other (mass difference less than 5 GeV) and the case where they are farther apart (mass difference greater than 5 GeV), we perform two searches as described below.

9.1 Search for an Additional State Taking the Observed SM Higgs-Like State as a Background

In this search, we set the observed state as a background process, let its mass and strength float, and simply look for a second excess. Exclusion limits on its signal strength μ and the associated p-value can be calculated in the same way as in the one-Higgs search. As

shown in Figure 9.1, once sufficiently away from 125 GeV, we recover the same exclusion limit as the one-Higgs search as expected. Since the observed state at 125 GeV is treated as a background, the region within ±5 GeV of 125 GeV is not used in the search. At 125 GeV, the limit does not go to infinity (i.e., the exclusion power is not zero) because when computing the limit, one cares about how the background can fluctuate downward to accommodate potential signal. Since the background cannot be negative, the deterioration in the exclusion power is finite. An additional SM-like Higgs is excluded everywhere except from 134.5 GeV to 137.5 GeV. The p-value at the most excess point, 136.5 GeV, is found to be 2.93. We also include a version of the limit plot where the y-axis is the absolute $\sigma\times$BR instead of the signal strength modifier μ (Figure 9.2).

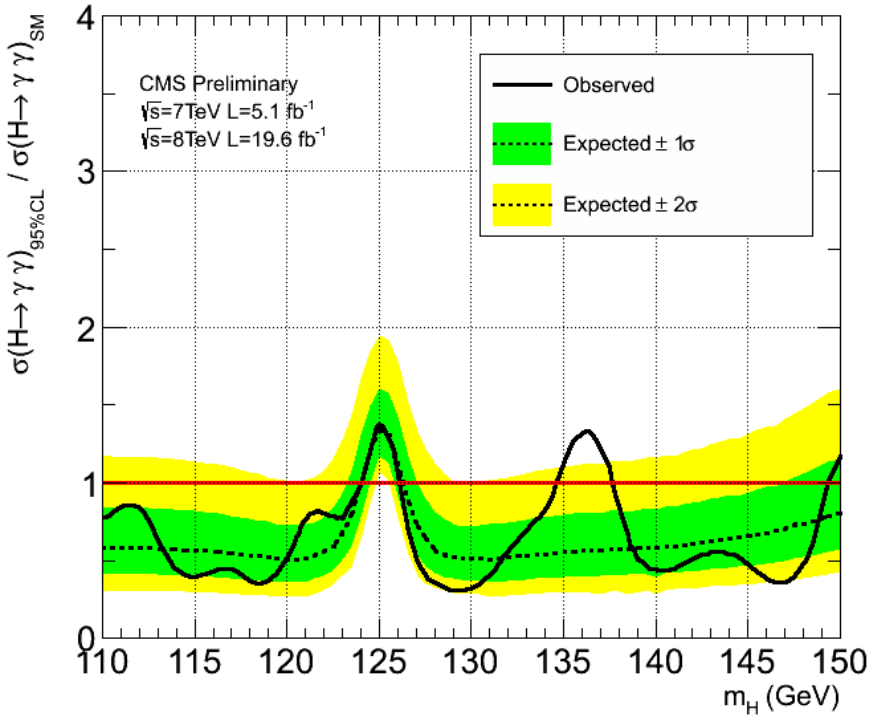

Figure 9.1: Exclusion limit (95% CL) for an additional SM-like Higgs state, taking the observed state as background and letting its signal strength and mass float.

In a more realistic scenario, i.e. in the alignment limit of the 2HDM scenarios, the additional state comes from a different composition of the various production mechanisms

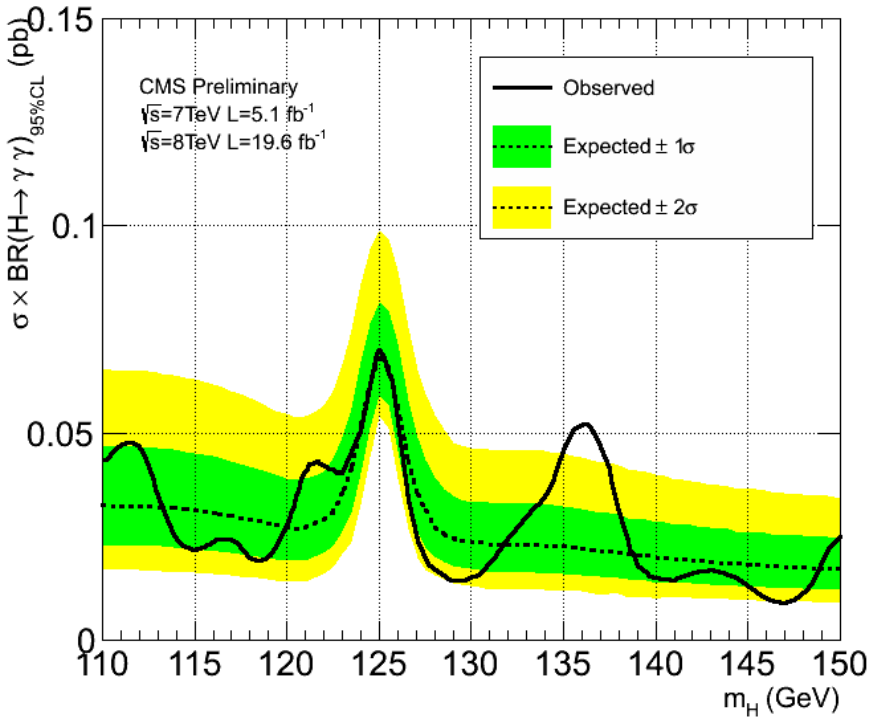

Figure 9.2: Exclusion limit (95% CL) on $\sigma \times$BR for an additional SM-like Higgs boson, taking the observed state as background and letting its signal strength and mass float.

from the SM Higgs boson. The alignment limit is defined as $\sin^2(\beta - \alpha) = 1$, where α and β are the two mixing angles in 2HDMs. In this limit, h has SM couplings, whereas H/A decouple from W and Z (gauge-phobic). Therefore for H and A, the only relevant production mechanism is gluon-fusion, which will be considered as the exclusive production mode for the additional state. Figure 9.3 shows the 95% CL exclusion limit on the $\sigma\times$BR for this search. The p-value at 136.5 GeV is found to be 2.73.

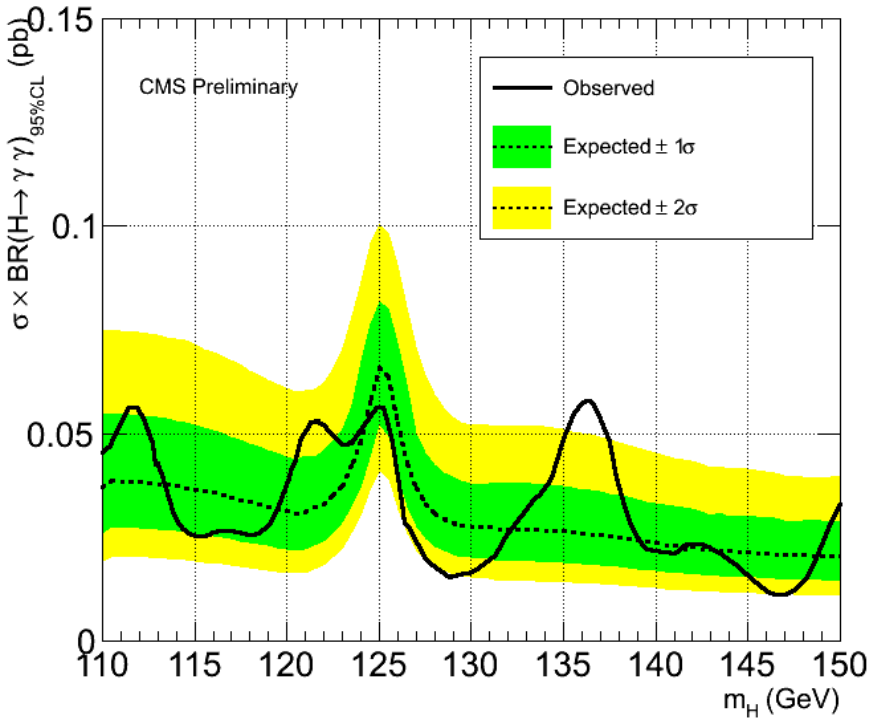

Figure 9.3: Exclusion limit (95% CL) on $\sigma\times$BR for an additional Higgs boson in the 2HDM alignment limit, taking the observed state as background and letting its signal strength and mass float. The additional Higgs boson is assumed to have only the gluon-fusion production mode.

In another scenario where the additional state is fermiophobic, we shall only consider vector boson fusion and W/Z associated production modes for the additional state. Figure 9.4 shows the 95% CL exclusion limit on the $\sigma\times$BR for this search. The p-value at 136.5 GeV is found to be 2.15.

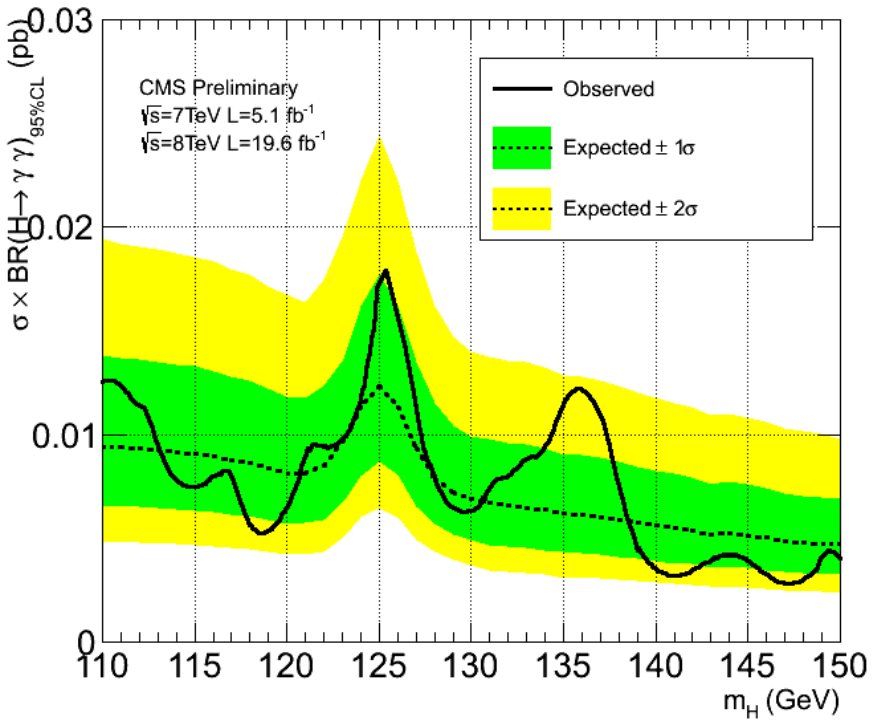

Figure 9.4: Exclusion limit (95% CL) on $\sigma \times$BR for an additional Higgs boson, taking the observed state as background and letting its signal strength and mass float. The additional Higgs boson is assumed to have only the vector boson fusion and W/Z associated production modes.

9.2 Search for Two Near-Degenerate States

The range of this search is limited to a window of a few GeV around the observed state at 125 GeV. Because of the high resolution of the diphoton channel, this search can be a powerful way to discriminate between a single Higgs boson at 125 GeV and two very close-by ones. The model is based on the one-Higgs search event selections and signal model, but re-parameterized in a way such that two mass variables, M_H and $M_{H2} = M_H + \Delta m$, point to two identical but independent sets of signal models. The relative strengths of the two signals are left to float, parameterized to be $r \times x$ and $r \times (1 - x)$, respectively, where r is now the total signal strength and x is the fraction of M_H. Δm is always positive and its range is [0 GeV, 5 GeV], whereas the range of x is [0, 1].

Note that in this parameterization, M_H is always on the left, with fraction x. Therefore, for x less than 0.5, the signal on the left is weaker than the signal on the right, and vice-versa.

Then, a 2D negative log-likelihood scan with respect to Δm and x is obtained by profiling over M_H and r. We expect to be sensitive for regions where Δm is greater than the experimental mass resolution and where both signal strengths are significant. Eventually, exclusion limits on Δm and x can be translated into exclusion limits on the mixing angles, and can serve as constraints on new physics.

Figure 9.5 shows the expected exclusion limit for this search, where the toy data is generated assuming one SM Higgs at 125 GeV and no additional state. As expected, scenarios where there are two comparable signals with a large mass separation are strongly disfavored. Figure 9.6 shows the observed exclusion limit from fitting the data. The observed data strongly disfavors cases where the state on the left is between and 2 and 5 times the rate of the state on the right, with a mass separation of at least 4 GeV.

9.3 Link to Parameters in 2HDMs

We can also translate limits in the Δm - x space to a space of Δm and β. We can treat the two signals we fit separately as: 1. H and h; 2. A and h, and exclude parameter spaces in

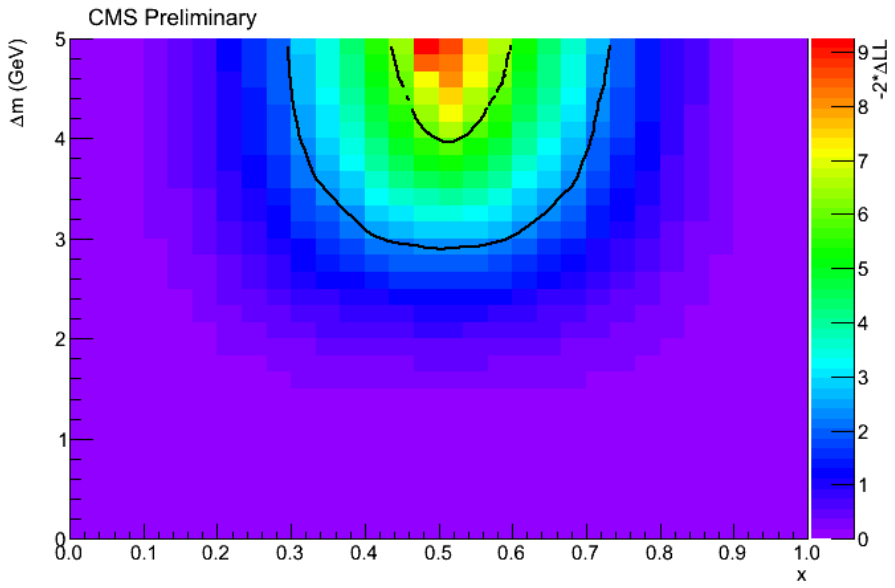

Figure 9.5: Expected exclusion limit for two near mass-degenerate states, in the scenario where there is only one Higgs at 125 GeV, with $\mu = 1$. The contours correspond to 68% and 95% CL. In this context, scenarios where the state on the left is between 2/3 and 3/2 times the rate of the state on the right and where the mass separation is at least 4 GeV are strongly disfavored.

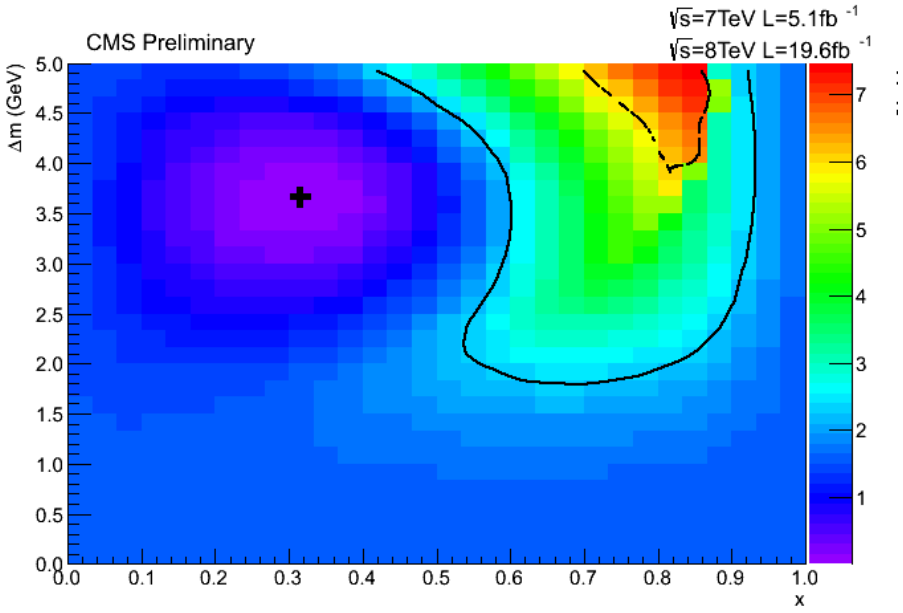

Figure 9.6: Observe exclusion limit for two near mass-degenerate states. The contours correspond to 68% and 95% CL. The black cross represents the best fit value. The skewness of the plot corresponds to the wider left shoulder on the one-Higgs limit plot. Data strongly disfavors cases where the state on the left is between and 2 and 5 times the rate of the state on the right, with a mass separation of at least 4 GeV.

the 2HDMs alignment limit.

Figures 9.7 and 9.8 show the exclusion limits for β (in radians) and Δm (in GeV) in the alignment limit, assuming the additional state is H and A, respectively. For a mass separation of 4.5 GeV or larger, we can exclude regions of β from $\pi/6$ to $\pi/8$ at 68% CL. The excluded space in the A/h scenario is larger than the H/h scenario, because A couples more strongly to photons. The numerical values that relate x to β are provided by Scott Thomas and Nathaniel Craig [22].

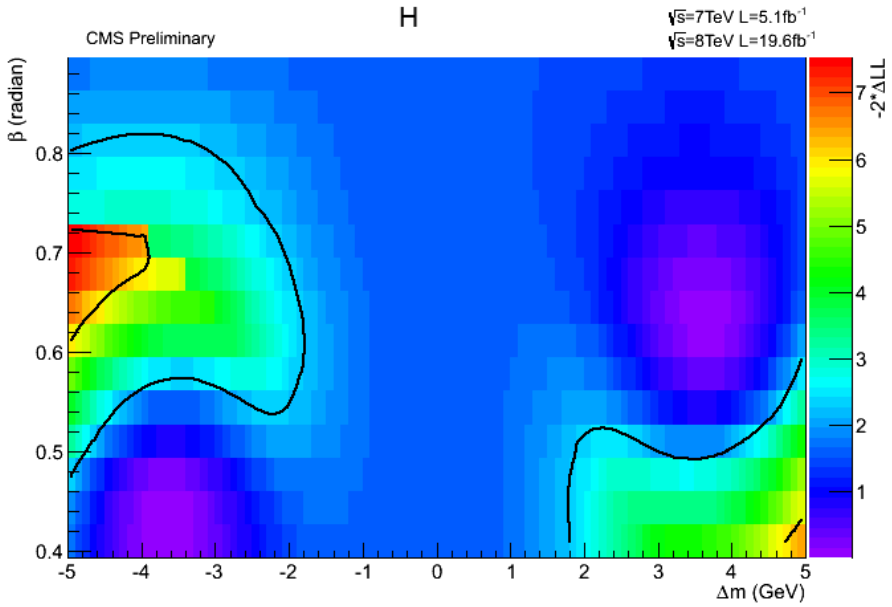

Figure 9.7: Exclusion limit for β (in radians) and Δm (in GeV) in the alignment limit, assuming the additional state is H. The contours correspond to 68% and 95% CL.

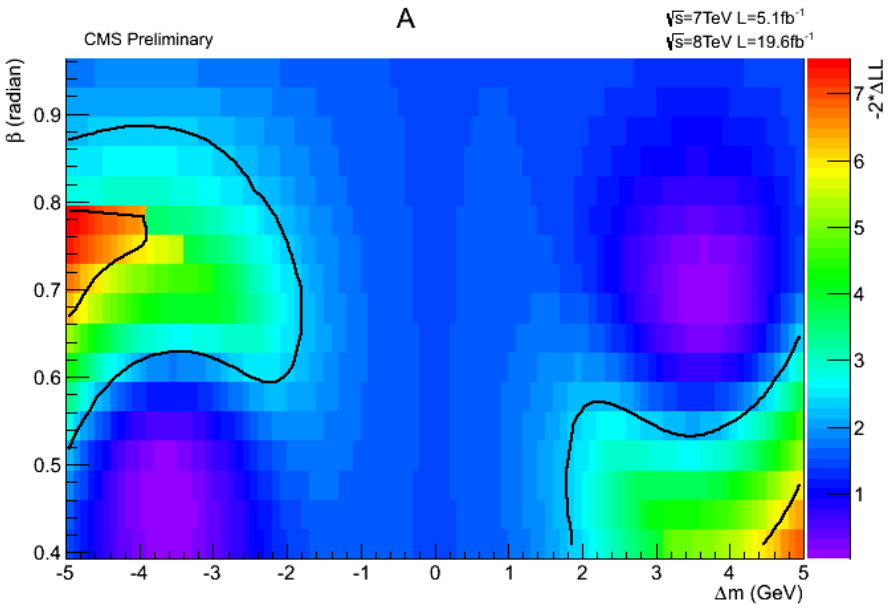

Figure 9.8: Exclusion limit for β (in radians) and Δm (in GeV) in the alignment limit, assuming the additional state is A. The contours correspond to 68% and 95% CL.

Chapter 10

Conclusion

Searches for a Standard Model Higgs Boson decaying into two photons have been performed using data obtained from 5.1 fb^{-1} and 19.6 fb^{-1} of pp collisions at $\sqrt{s}$=7 TeV and at $\sqrt{s}$=8 TeV, respectively. For the MVA analysis, the selected events are subdivided into classes according to indicators of mass resolution and predicted signal-to-background ratio, and the results of a search in each class are combined. The expected sensitivity on the limit on the production cross-section times branching fraction($\sigma\times$BR), at 95% confidence level, is between 0.48 and 0.76 times the SM prediction in the mass range 110-150 GeV. Results obtained from the crosscheck cut-based analysis are also reported and are consistent with those from the MVA analysis.

An excess of events above the expected standard model background is observed for a Higgs boson mass hypothesis of 125 GeV, where the expected limit is 0.48 times the standard model expectation. The local significance of this excess is 3.2σ. This result constitutes further evidence for the existence of a new massive state that decays into two photons. The mass of the observed boson is measured to be $125.4 \pm 0.5(stat.) \pm 0.6(syst.)$ GeV. For a Higgs boson mass hypothesis of 125 GeV, the best fit signal strength is $0.78^{+0.28}_{-0.26}$ times the SM Higgs boson cross-section. We set an upper limit on the natural width of the observed boson, measured to be 6.9 GeV/c^2.

We also present results from searches for an additional Higgs boson decaying into two

photons, treating the observed resonance as a background process. Cases in which the additional state is SM-like, fermiophobic or gauge-phobic have been considered. Exclusions limits on the $\sigma\times$BR of the additional state are reported for each scenario.

In addition, we present a search targeted at discriminating between a single Higgs boson at 125 GeV and two very close-by ones. We exclude scenarios where the state on the left is between and 2 and 5 times the rate of the state on the right, with a mass separation of at least 4 GeV. In the alignment limit scenario, where the additional state decouples from gauge bosons, we can exclude regions of β from $\pi/6$ to $\pi/8$ at 68% CL.

References

[1] V. Ghete, "The CMS L1 Trigger Emulation Software". 17th International Conference on Computing in High Energy and Nuclear Physics (2009).

[2] The CMS $H \to \gamma\gamma$ working group, "Search for a Higgs boson decaying into two photons in pp collisions recorded by the CMS detector at the LHC". CMS Analysis Note 2011/426(2011).

[3] S. L. Glashow, "Partial Symmetries of Weak Interactions," Nucl. Phys. **22**, 579 (1961).

[4] S. Weinberg, "A Model of Leptons," Phys. Rev. Lett. **19**, 1264 (1967).

[5] A. Salam, "Weak and Electromagnetic Interactions," Conf. Proc. C **680519**, 367 (1968).

[6] F. Englert and R. Brout, "Broken Symmetry and the Mass of Gauge Vector Mesons," Phys. Rev. Lett. **13**, 321 (1964).

[7] P. W. Higgs, "Broken symmetries, massless particles and gauge fields," Phys. Lett. **12**, 132 (1964).

[8] P. W. Higgs, "Broken Symmetries and the Masses of Gauge Bosons," Phys. Rev. Lett. **13**, 508 (1964).

[9] G. S. Guralnik, C. R. Hagen and T. W. B. Kibble, "Global Conservation Laws and Massless Particles," Phys. Rev. Lett. **13**, 585 (1964).

[10] P. W. Higgs, "Spontaneous Symmetry Breakdown without Massless Bosons," Phys. Rev. **145**, 1156 (1966).

[11] T. W. B. Kibble, "Symmetry breaking in nonAbelian gauge theories," Phys. Rev. **155**, 1554 (1967).

[12] M. Maggiore, "A Modern introduction to quantum field theory," Oxford University Press, 2005. (Oxford Series in Physics, 12. ISBN 0 19 852073 5)

[13] J. F. Gunion, H. E. Haber, G. L. Kane and S. Dawson, "The Higgs Hunter's Guide," Front. Phys. **80**, 1 (2000).

[14] M. Spira, A. Djouadi, D. Graudenz and P. M. Zerwas, "Higgs boson production at the LHC," Nucl. Phys. B **453**, 17 (1995) [hep-ph/9504378].

[15] R. V. Harlander and W. B. Kilgore, "Next-to-next-to-leading order Higgs production at hadron colliders," Phys. Rev. Lett. **88**, 201801 (2002) [hep-ph/0201206].

[16] S. Dittmaier *et al.* [LHC Higgs Cross Section Working Group Collaboration], "Handbook of LHC Higgs Cross Sections: 1. Inclusive Observables," arXiv:1101.0593 [hep-ph].

[17] S. Dittmaier, S. Dittmaier, C. Mariotti, G. Passarino, R. Tanaka, S. Alekhin, J. Alwall and E. A. Bagnaschi *et al.*, "Handbook of LHC Higgs Cross Sections: 2. Differential Distributions," arXiv:1201.3084 [hep-ph].

[18] S. Actis, G. Passarino, C. Sturm and S. Uccirati, "NNLO Computational Techniques: The Cases H $\rightarrow$ gamma gamma and H $\rightarrow$ g g," Nucl. Phys. B **811**, 182 (2009) [arXiv:0809.3667 [hep-ph]].

[19] J. Ellis, J. R. Espinosa, G. F. Giudice, A. Hoecker and A. Riotto, "The Probable Fate of the Standard Model," Phys. Lett. B **679**, 369 (2009) [arXiv:0906.0954 [hep-ph]].

[20] J. Alcaraz [ALEPH and CDF and D0 and DELPHI and L3 and OPAL and SLD Collaboration], "Precision Electroweak Measurements and Constraints on the Standard Model," arXiv:0911.2604 [hep-ex].

[21] G. C. Branco, P. M. Ferreira, L. Lavoura, M. N. Rebelo, M. Sher and J. P. Silva, "Theory and phenomenology of two-Higgs-doublet models," Phys. Rept. **516**, 1 (2012) [arXiv:1106.0034 [hep-ph]].

[22] N. Craig and S. Thomas, "Exclusive Signals of an Extended Higgs Sector," JHEP **1211**, 083 (2012) [arXiv:1207.4835 [hep-ph]].

[23] L. Evans and P. Bryant, "LHC Machine," JINST **3**, S08001 (2008).

[24] S. Chatrchyan *et al.* [CMS Collaboration], "The CMS experiment at the CERN LHC," JINST **3**, S08004 (2008).

[25] G. L. Bayatian *et al.* [CMS Collaboration], "CMS physics: Technical design report," CERN-LHCC-2006-001.

[26] G. L. Bayatian *et al.* [CMS Collaboration], "CMS technical design report, volume II: Physics performance," J. Phys. G **34**, 995 (2007).

[27] S. Dasu *et al.* [CMS Collaboration], "CMS. The TriDAS project. Technical design report, vol. 1: The trigger systems," CERN-LHCC-2000-038.

[28] [CMS Collaboration], "CMS: The Electromagnetic Calorimeter. Technical design report," CERN-LHCC-97-33.

[29] A. Bornheim [CMS ECAL Collaboration], "The CMS ECAL laser monitoring system," AIP Conf. Proc. **867**, 408 (2006).

R. Arcidiacono [CMS ECAL Collaboration], "Studies of the CMS electromagnetic calorimeter performance in the electron test beam," J. Phys. Conf. Ser. **160**, 012048 (2009).

[30] S. Chatrchyan *et al.* [CMS Collaboration], "Energy calibration and resolution of the CMS electromagnetic calorimeter in pp collisions at $\sqrt{s} = 7$ TeV," arXiv:1306.2016 [hep-ex].

[31] S. Agostinelli *et al.* [GEANT4 Collaboration], "GEANT4: A Simulation toolkit," Nucl. Instrum. Meth. A **506**, 250 (2003).

[32] [CMS Collaboration], "Commissioning of the Particle-Flow Event Reconstruction with the first LHC collisions recorded in the CMS detector", CDS Record **1247373**(2010).

[33] M. Cacciari and G. P. Salam, "Pileup subtraction using jet areas," Phys. Lett. B **659**, 119 (2008) [arXiv:0707.1378 [hep-ph]].

[34] [CMS Collaboration], "Trigger strategies for Higgs searches in 2011, CMS Analysis Note, CMS-AN-11-065 (2011).

[35] C. Tully, V. Rekovic, X. Quan, "Photon Trigger Paths for the $H \to \gamma\gamma$ Search at Instantaneous Luminosities of 5e32 to 5e33 $\mathrm{cm}^{-2}\mathrm{s}^{-1}$". CMS Analysis Note, CMS-AN-10-353(2010).

[36] V. Khachatryan *et al.* [CMS Collaboration], "Measurements of Inclusive W and Z Cross Sections in pp Collisions at $\sqrt{s} = 7$ TeV," JHEP **1101**, 080 (2011) [arXiv:1012.2466 [hep-ex]].

[37] [CMS Collaboration], "Photon reconstruction and identification at $\sqrt{s} = 7$ TeV", CMS Physics Analysis Summary, CMS-PAS-EGM-10-005(2010).

[38] M. Anderson, A. Askew,A. F. Barfuss, D. Evans, F. Ferri, K. Kaadze, Y. Maravin, P. Meridiani, C. Seez, "Review of clustering algorithms and energy corrections in ECAL", IN-2010/008(2010).

[39] A. Hocker, J. Stelzer, F. Tegenfeldt, H. Voss, K. Voss, A. Christov, S. Henrot-Versille and M. Jachowski *et al.*, "TMVA - Toolkit for Multivariate Data Analysis," PoS ACAT , 040 (2007) [physics/0703039 [PHYSICS]].

[40] S. Chatrchyan *et al.* [CMS Collaboration], "Search for the standard model Higgs boson decaying into two photons in *pp* collisions at $\sqrt{s} = 7$ TeV," Phys. Lett. B **710**, 403 (2012) [arXiv:1202.1487 [hep-ex]].

[41] [CMS Collaboration], "Updated measurements of the Higgs-like boson at 125 GeV in the two photon decay channel", CMS Physics Analysis Summary, CMS-PAS-HIG-13-001(2013).

[42] [CMS Collaboration],"Updated measurements of the Higgs-like boson at 125 GeV in the two photon decay channel", CMS Analysis Note, CMS-AN-13-008(2013).

[43] G. Cowan, K. Cranmer, E. Gross and O. Vitells, "Asymptotic formulae for likelihood-based tests of new physics," Eur. Phys. J. C **71**, 1554 (2011) [arXiv:1007.1727 [physics.data-an]].

[44] A. L. Read, "Presentation of search results: The CL(s) technique," J. Phys. G **28**, 2693 (2002).

[45] [ATLAS and CMS Collaboration], "Procedure for the LHC Higgs boson search combination in Summer 2011", CMS Note, CMS-NOTE-2011-005(2011).

[46] [CMS Collaboration], "Evidence for a new state decaying into two photons in the search for the standard model Higgs boson in pp collisions", CMS Physics Analysis Summary, CMS-PAS-HIG-12-015(2013).

[47] S. Chatrchyan *et al.* [CMS Collaboration], "Observation of a new boson at a mass of 125 GeV with the CMS experiment at the LHC," Phys. Lett. B **716**, 30 (2012) [arXiv:1207.7235 [hep-ex]].

[48] G. Aad *et al.* [ATLAS Collaboration], "Observation of a new particle in the search for the Standard Model Higgs boson with the ATLAS detector at the LHC," Phys. Lett. B **716**, 1 (2012) [arXiv:1207.7214 [hep-ex]].

[49] G. J. Feldman and R. D. Cousins, "A Unified approach to the classical statistical analysis of small signals," Phys. Rev. D **57**, 3873 (1998) [physics/9711021 [physics.data-an]].

[50] G. Degrassi, S. Di Vita, J. Elias-Miro, J. R. Espinosa, G. F. Giudice, G. Isidori and A. Strumia, "Higgs mass and vacuum stability in the Standard Model at NNLO," JHEP **1208**, 098 (2012) [arXiv:1205.6497 [hep-ph]].